AFRL-AFOSR-VA-TR-2020-0060

Aramid Nanofiber - Functionalized Graphene Electrode for Structural Energy and Power

Jodie Lutkenhaus
TEXAS ENGINEERING EXPERIMENT STATION COLLEGE STATION

03/13/2020
Final Report

Air Force Research Laboratory
AF Office Of Scientific Research (AFOSR)/ RTA1
Arlington, Virginia 22203
Air Force Materiel Command

REPORT DOCUMENTATION PAGE

Form Approved
OMB No. 0704-0188

1. REPORT DATE *(DD-MM-YYYY)*	2. REPORT TYPE	3. DATES COVERED *(From - To)*
11-06-2020	Final Performance	15 May 2016 to 14 Nov 2019

4. TITLE AND SUBTITLE
Aramid Nanofiber - Functionalized Graphene Electrode for Structural Energy and Power

5a. CONTRACT NUMBER

5b. GRANT NUMBER
FA9550-16-1-0230

5c. PROGRAM ELEMENT NUMBER
61102F

6. AUTHOR(S)
Jodie Lutkenhaus, Dimitris Lagoudas

5d. PROJECT NUMBER

5e. TASK NUMBER

5f. WORK UNIT NUMBER

7. PERFORMING ORGANIZATION NAME(S) AND ADDRESS(ES)
TEXAS ENGINEERING EXPERIMENT STATION COLLEGE STATION
1470 WILLIAM D FITCH PKY
COLLEGE STATION, TX 77843-3577 US

8. PERFORMING ORGANIZATION REPORT NUMBER

9. SPONSORING/MONITORING AGENCY NAME(S) AND ADDRESS(ES)
AF Office of Scientific Research
875 N. Randolph St. Room 3112
Arlington, VA 22203

10. SPONSOR/MONITOR'S ACRONYM(S)
AFRL/AFOSR RTA1

11. SPONSOR/MONITOR'S REPORT NUMBER(S)
AFRL-AFOSR-VA-TR-2020-0060

12. DISTRIBUTION/AVAILABILITY STATEMENT
A DISTRIBUTION UNLIMITED: PB Public Release

13. SUPPLEMENTARY NOTES

14. ABSTRACT

The research instrumentation funds have been used to build a computer-instrumented and computer-controlled experimental apparatus that emulates the combustor a gas turbine engine. This test apparatus will be specifically designed to be capable of emulating nominal and some of the critical anticipated & unanticipated off-nominal transient operating conditions as well as emergency situations in typical combustors of aircraft gas turbine engines. The apparatus also serves as a test bed for early prediction and real-time active control of (emulated) combustion instabilities in aircraft gas turbine engines
From the above perspective, the requested instrumentation has supported and will continue to support experimental validation of the results of theoretical research in dynamic data-driven application systems (DDDAS), which include algorithms of:
Real-time knowledge extraction from heterogeneous dynamic data in stochastic settings;
Reduced-order modeling trained by experimental data of spatio-temporal dynamics;
Machine learning and information fusion at multiple scales of space and time; and
Uncertainty quantification in real-time prediction & control of combustion instabilities.

15. SUBJECT TERMS
structural batteries, Functionalized Graphene Electrode, Aramid Nanofiber

16. SECURITY CLASSIFICATION OF:			

a. REPORT	b. ABSTRACT	c. THIS PAGE	17. LIMITATION OF ABSTRACT	18. NUMBER OF PAGES	19a. NAME OF RESPONSIBLE PERSON
Unclassified	Unclassified	Unclassified	UU		BIRKAN, MITAT
					19b. TELEPHONE NUMBER *(Include area code)* 703-696-7234

REPORT DOCUMENTATION PAGE

Form Approved
OMB NO. 0704-0188

1. AGENCY USE ONLY (Leave Blank)	2. REPORT DATE March 13, 2020	3. REPORT TYPE AND DATES COVERED Final Report from March 01, 2018 to Feb 28, 2020

4. Test Bed for Dynamic Data-Driven Feature Extraction and Information Fusion in Combustion Systems of Aircraft Gas Turbine Engines **5.** Subtitle: None	5. FUNDING NUMBERS Award No. FA9550-18-1-0135
6. AUTHOR(S) Asok Ray	
7. PERFORMING ORGANIZATION NAME(S) AND ADDRESS(ES) The Pennsylvania State University, University Park, PA 1680	8. PERFORMING ORGANIZATION Pennsylvania State University
9. SPONSORING / MONITORING AGENCY NAME(S) AND ADDRESS(ES) Dr. Erik Blasch Air Force Office of Scientific Research	10. SPONSORING / MONITORING AGENCY REPORT NUMBER REPORT NUMBER DURIP 2017/Ray

11. SUPPLEMENTARY NOTES
The views, opinions and/or findings contained in this report are those of the author(s) and should not be construed as an official Department of the Army position, policy or decision, unless so designated by other documentation.

12 a. DISTRIBUTION / AVAILABILITY STATEMENT	12 b. DISTRIBUTION CODE
Approved for public release; distribution unlimited.	UL.

13. ABSTRACT (Maximum 200 words)

The Pennsylvania State University has developed the (wireless) Networked Robotic Systems Laboratory (NRSL) under several Defense University Instrumentation Program (DURIP) grants. The objective is to experimentally validate the results of theoretical research on mathematics of anomalous behavior in sensor-network-based miniature multimodal mobile robots and electromechanical systems.

The procured instrumentation has augmented the existing Networked Robotic Systems Laboratory (NRSL) (web address: http://nrsl.mne.psu.edu/) that has served previous Multidisciplinary University Research Initiative (MURI) projects (ARO Grant Nos. DAAD19-01-1-0646 and W911NF-07-1-0376) for sensor fusion research on networked robotic platforms. The research instrumentation has also supported the activities of an Army Research Laboratory (ARL) project (Grant No. W911NF-14-2-0068) and other ongoing DoD research projects at Penn State, such as AFOSR Grant Nos. FA9550-12-1-0270 and FA9550-15-1-0400 as well as an ONR project (Grant No. N00014-14-1-0545).

The instrumentation equipment procured under the 2015 DURIP grant interfaces with those of the 2013 DURIP and earlier DURIP grant equipment and other existing facilities of Pennsylvania State University (PSU). The individual units of NRSL are interconnected over an internet and are supplemented with a wireless network of stationary and mobile processing platforms to analyze the effects of failure propagation in networked complex systems.

14. SUBJECT TERMS			15. NUMBER OF PAGES 51
			16. PRICE CODE
17. SECURITY CLASSIFICATION OR REPORT **UNCLASSIFIED**	18. SECURITY CLASSIFICATION ON THIS PAGE **UNCLASSIFIED**	19. SECURITY CLASSIFICATION OF ABSTRACT **UNCLASSIFIED**	20. LIMITATION OF ABSTRACT **UL**

Final Report
on

2017 Defense University Research Instrumentation Program

4. Test Bed for Dynamic Data-Driven Feature Extraction and Information Fusion

in Combustion Systems of Aircraft Gas Turbine Engines

Research Agreement No. W911NF-15-1-0369

Starting Date:	March 01, 2018
End date:	February 28, 2020
Recipient University:	The Pennsylvania State University (PSU)
Program Manager:	Dr. Erik Blasch, Air Force Office of Scientific Research
Principal Investigator:	Professor Asok Ray, Penn State

March 13, 2020

Introduction

The research instrumentation funds have been used to build a computer-instrumented and computer-controlled experimental apparatus that emulates the combustor a gas turbine engine. This test apparatus will be specifically designed to be capable of emulating nominal and some of the critical anticipated & unanticipated off-nominal transient operating conditions as well as emergency situations in typical combustors of aircraft gas turbine engines. The apparatus also serves as a test bed for early prediction and real-time active control of (emulated) combustion instabilities in aircraft gas turbine engines

From the above perspective, the requested instrumentation has supported and will continue to support experimental validation of the results of theoretical research in dynamic data-driven application systems (DDDAS), which include algorithms of:

- Real-time knowledge extraction from heterogeneous dynamic data in stochastic settings;
- Reduced-order modeling trained by experimental data of spatio-temporal dynamics;
- Machine learning and information fusion at multiple scales of space and time; and
- Uncertainty quantification in real-time prediction & control of combustion instabilities.

Existing combustion test apparatuses at different universities and research laboratories are designed to operate under constrained conditions that do not allow the transients of many off-nominal operations and emergency situations; therefore, the proposed apparatus would be useful for experimental validation of the above-mentioned algorithms under various (emulated) operating conditions in a laboratory environment. The test apparatus will be designed to be flexible for future expansion into a fully equipped combustor for handling operating conditions that other existing apparatuses may not be able to accommodate. This apparatus will support an ongoing DDDAS research project (AFOSR Grant No. FA9550-15-1-0400) and several other research projects. In addition to validation of research results to advance the state-of-the-art in DDDAS, the experimental apparatus will be used for instruction of current and new graduate & undergraduate courses in conjunction with other educational apparatuses at Penn State laboratories.

Application to Defense Requirements

The research in the laboratory addresses fundamentally new approaches to designing and operating fault-tolerant sensing and decision systems for multiple concurrent applications. Specifically, the research will provide a scientific and technical base for dynamic utilization of redundancy through information-theoretic analysis depending on the instantaneous state of components. The ultimate benefits of this research are to enhance operational reliability and preparedness of the U.S. military.

From the perspectives of health management of plant structures and its fleet-wide implementation in the battlefield environment, major benefits of the proposed research are enhanced safety, reliability, and availability; reduction of the life cycle cost by optimization of the operation and maintenance schedule; and reduced need for skilled technicians for on-site maintenance.

Estimated Useful Life of the Equipment

The estimated useful life of different categories of equipment is delineated below:

- *Complex Systems Emulation Equipment*: The average life of equipment in this category is estimated to be about ten years because the technology in this field is evolving at rapid pace.

- *Thermal-hydraulic and Combustion System Emulation, and Visualization Equipment*: The average life of equipment in this category of robotic equipment is estimated to be about twenty years because the technology in this field is moderately mature and is evolving at medium pace

Property Report

All equipment procured under the Research Award No. **FA9550-18-1-0135** vests with Pennsylvania State University that is the sole recipient of this DURIP award.

Budget Report

The total budget of this research equipment project (Grant No. W911NF-15-1-0369) is **$272,530.00**, which is completely funded by the DoD. The current expenses for equipment purchase has been approximately **$200,906.00**. The remaining amount of approximately **$71,624.00** has been used for supporting the salaries of the engineer and technicians for laboratory construction.

APPENDIX

Following archive journal publications have been generated on the experimental apparatus:

S. Mondal, N.F. Ghalyan, A. Ray and A. Mukhopadhyay, "Early Detection of Thermoacoustic Instabilities Using Hidden Markov Models," Combustion Science and Technology, vol. 191, no. 8, August 2019, pp. 1309-1336. doi: 10.1080/00102202.2018.1523900

C. Bhattacharya, S. Mondal, A. Ray and A. Mukhopadhyay, "Reduced-order Modeling of Thermoacoustic Instabilities in a Two-heater Rijke Tube, " Combustion Theory and Modeling, in press. doi: 10.1080/13647830.2020.1714080

COMBUSTION SCIENCE AND TECHNOLOGY
2019, VOL. 191, NO. 8, 1309–1336
https://doi.org/10.1080/00102202.2018.1523900

Taylor & Francis
Taylor & Francis Group

ARTICLE

Early Detection of Thermoacoustic Instabilities Using Hidden Markov Models

Sudeepta Mondal[a], Najah F. Ghalyan[a], Asok Ray[a,b], and Achintya Mukhopadhyay[c]

[a]Department of Mechanical Engineering, The Pennsylvania State University, University Park, PA, USA; [b]Department of Mathematics, The Pennsylvania State University, University Park, PA, USA; [c]Department of Mechanical Engineering, Jadavpur University, Kolkata, India

ABSTRACT

This paper presents a dynamic data-driven method for early detection of thermoacoustic instabilities in combustors based on short-length time series of sensor data, where the objective is near-real-time monitoring and active control of pressure oscillations. The main idea is to use the available data at different regimes of the combustion process to train respective hidden-variable models using the concept of Hidden Markov Modeling (HMM) as a statistical learning tool; here, (short-length) time-series data of pressure oscillations are used to infer a Markov chain with unobserved (hidden) states. The proposed HMM-based method has been validated on experimental data collected from an electrically heated Rijke tube apparatus for predicting onset of thermoacoustic instabilities. The results have been compared with those of the current state-of-the-art measurement techniques for instability growth rate and associated computational complexity. The applicability of the proposed method has been demonstrated with respect to anomaly detection and regime identification with limited data requirements, making it a potential candidate for monitoring and active control of thermoacoustic instabilities in commercial-scale combustors.

ARTICLE HISTORY
Received 9 June 2018
Revised 11 September 2018
Accepted 11 September 2018

KEYWORDS
Thermoacoustic instability; hidden Markov modeling; real-time monitoring; active control

Introduction

Thermoacoustic instabilities (TAI) in combustion systems are related to spontaneous excitation of one or more natural acoustic modes (Lieuwen and Yang, 2005). These phenomena are typically manifested by large-amplitude self-sustained pressure oscillations in the combustion chamber, which result from a feedback loop established between the heat release rate from the flame and the combustion chamber acoustics (Matveev, 2003). A major detrimental effect of TAI is resonance, which may occur if the frequency of pressure oscillations matches the natural frequency of the combustor chamber; in that case, sustained high-amplitude pressure and temperature oscillations would cause severe mechanical stresses in the structural components of the combustor, leading to thermomechanical fatigue damage and premature structural failures.

Another detrimental effect of TAI is generation of externally audible tones at intolerable levels. Hence, mitigation of TAI is a critical issue from the perspectives of both design and operation of combustion systems.

CONTACT Asok Ray axr2@psu.edu Department of Mechanical Engineering, Pennsylvania State University, University Park, PA 16802, USA

One of the major reasons for application of active TAI control techniques is their potential for adaptability to various operational regimes of the combustion process, without compromising the weight requirements of an aircraft engine. A necessary precondition for such near-real-time active control is early detection of forthcoming TAI by making use of the available sensor time-series data. This detection problem would require system identification (e.g., accurate estimation of the degree of instability) from the sensor data at fast time scales for near-real-time decision and control. The rationale is that the time scales of TAI are in milliseconds, which mandates the requirement of system identification with short data and low computational complexity of the underlying algorithms (Mukherjee and Ray, 2014; Rajagopalan and Ray, 2006; Ray, 2004; Sarkar et al., 2016) for monitoring and active control.

From the perspectives of dynamical systems, the phenomena of TAI occur due to nonlinear triggering by Hopf bifurcations. In this respect, it is a well-known practice to characterize stable/unstable operational regimes in terms of the distance from the Hopf bifurcation point by using system growth/damping rates. In this context, positive growth rate of an acoustic mode implies that it is unstable with its fluctuation amplitude growing exponentially with time. On the other hand, an acoustic mode with a negative growth rate has perturbations decaying with time (Laera et al., 2014). The growth rate information can be used directly to quantify the distance of the current operating point from the point of TAI onset. An efficient method for online monitoring of the stability margin is crucial for the decision-maker (e.g., an automated system or a human operator) to make informed decisions about changing the operating conditions, based on the existing prior knowledge of the stability map with respect to the system parameters. Such methods are passive in the sense that they should not require external stimulation to be applied on the combustion systems (Lieuwen, 2005). Several researchers have addressed this issue by developing methods of calculating the linear growth/damping rates based on sensor data of the acoustic signature of the combustion process (e.g., Hummel et al., 2017; Noiray and Denisov, 2017; Rigas et al., 2016; Li et al., 2016; Lieuwen, 2005; Yi and Gutmark, 2008).

To the best of the authors' knowledge, most of the above methods are only suitable for offline data-intensive computations, where the execution time of the underlying algorithms and their data requirements could cause large delays relative to the time scale of TAI, if applied for online condition monitoring and active control of combustion systems. Li et al. (2016) have chosen the total acoustic energy per unit cross-sectional area as a measure to characterize the transient growth. They have used physics-based modeling by modal analysis involving Galerkin decomposition. Although similar practices involving modal analysis are widely reported in literature, specifically with respect to Rijke tubes, it might be difficult to develop a model involving the complications of a wide range of parameters in an actual combustion system. Furthermore, the nonlinear and non-normal properties of such system models add to fragility (i.e., lack of robustness) of their dynamical behavior, which imply that a stable system may become unstable with a slight change in initial conditions and certain critical system parameters. Therefore, in practice, it would become difficult to specify and maintain initial conditions and critical parameters with respect to those in the modal analyses, which will complicate the calibration of these models. From these perspectives, dynamic data-driven techniques of growth rate extraction can be very useful, as they have limited dependency on the accuracy of physics-based models. Often the root mean square of the pressure signal (P_{rms}) is used as a simple measure to set a threshold for identifying the system instability. It is noted that P_{rms} also

refers to the square root of the average energy in the signal, which is closely related to the total acoustic energy approach used by Li et al. (2016). However, since the threshold may vary from one application to another, and if this concept is used for identification of operational regimes, it might be difficult to specify thresholds for different regimes with a wide range of signal-to-noise-ration (SNR) in the sensor data. Moreover, P_{rms}-based thresholds are mostly reliable only if the data are sufficiently long in order to satisfy the requirements of statistical stationarity (Mondal et al., 2017), which deems them unsuitable to be used as a unified framework for online TAI detection and regime identification.

Other techniques of growth rate measurement have been reported in the literature, which are based on system identification from acoustic data. For example, Noiray and Denisov (2017), Boujo et al. (2016), and Noiray and Schuermans (2012, 2013) have approximated the growth dynamics of the dominant unstable mode with stochastic differential equations (SDE) governing the amplitude and phase of a randomly forced Van der Pol oscillator, driven by additive noise. Subsequently, analytical stationary solutions to the Fokker-Plank equation associated with the SDEs have been used to describe the stationary probability distribution of the acoustic signal envelope, which involves coefficients to be fitted from the acoustic data to determine the growth rate of the oscillations. However, its applicability is expected to be limited for real-time applications, where estimation of the stationary probability distributions of the acoustic envelope would most likely be subject to a significant data requirement. In practice, it might be difficult to correlate the model parameters of a Van der Pol oscillator with those of a general combustion system in terms of their physical significance.

The technical approach of Lieuwen (2005) is somewhat different, where the extent of departure of the combustion system from its stability boundary is characterized by a decrease in the effective damping rate (ζ) of the system toward zero. The strategy is based on estimating the damping rate by performing least-squares minimization procedure to determine the best fit exponential curve $\exp(-\omega\zeta t)$ for an acoustic mode with frequency ω. Lieuwen (2005) has pointed out the limitation of this method with respect to the dependence of the estimation procedure of ζ upon the time delays of the autocorrelation function, and hence the length of the time series used for the estimation. The work by Hummel et al. (2017) and Stadlmair et al. (2017) is suited in a similar framework of estimating the damping rates through curve-fitting on the autocorrelation function derived from high frequency screech-level pressure oscillations at operating conditions, where the time-scale of variations in the amplitude and phase of the unstable mode are much slower relative to the oscillatory time scale. While the method of Lieuwen (2005) was based on the damping rate estimation in the time domain, Yi and Gutmark (2008) based their work of computing damping ratios of the acoustic modes in the frequency domain, starting with a similar model for the modal dynamics of the pressure oscillations as used by Lieuwen (2005). The damping ratios were determined by fitting a smooth curve on the frequency spectrum in the vicinity of the resonant frequency peaks using a weighted least-mean-square algorithm, by utilizing a sample length of 10,000 with a sampling frequency of 5 kHz. Such frequency-domain analyses using Fast Fourier transform (FFT)/Discrete Fourier transform typically require considerable sample points for efficient representations of the power spectral densities. Boujo et al. (2016) and Hummel et al. (2017) have based the identification procedure of growth rates for linearly unstable

cases on analytically solvable SDEs and then fitted the analytical solutions against the measured time-domain data. These SDE-based frameworks are suitable for estimating the growth rate from the stationary acoustic data at different operating conditions (e.g., different equivalence ratios); in contrast, the method developed in the current paper can be used to obtain running estimates of the triggering of transient growths involved in bifurcations that are essentially non-stationary in nature. Also, for almost all of the research literature surveyed, the quantitative determination of the growth/decay rates of combustion is not completely data-driven in the sense that they require simplified (i.e., linearized and the assumed additive noise) physics-based mathematical models of pressure oscillations, which in turn makes it difficult to justify generalization of these models to handle the problem of TAI prediction, because the underlying process is highly nonlinear and is subjected to non-additive noise.

This paper proposes a dynamic data-driven method for early detection of TAI and identification of operational regimes by using short-length time series of sensor data, which is robust to the following properties:

- Variations in the length of the observed time series, used for instability prediction and regime identification.
- Inadequacies of the underlying combustion system model if any such model is used.

The application domain of the work by Rigas et al. (2016), who have reported a growth rate measurement technique based on linear fitting on the Hilbert envelope of the unsteady pressure time-series data, is similar to the experimental data used in the current paper. The data requirements of the proposed method have been compared with those of (Rigas et al., 2016) .

Since the focal area of the reported work is early detection of instabilities, analyses have been performed using pressure time-series data that undergo transient behavior from a stable operation to limit-cycle oscillations. Furthermore, pressure sensing is commonly used in many real-life combustion systems. Thus, implementation using pressure data readily demonstrates suitability of the proposed method for practical situations. The main idea here is to use primarily experimentally generated acoustic sensor data from different regimes of the combustion process to train relevant hidden-variable models using the concept of hidden Markov modeling (HMM) (Rabiner, 1989) that has been widely used as a statistical learning tool for analysis of uncertain dynamical systems; in these applications, the associated temporal data are used to infer a Markov chain with unobserved states. For example, Menon et al. (2003) and Chen et al. (2011) have used the HMM concept for online predictive monitoring and fault detection in gas turbine engines. The trained HMM contains the latent information of the system's dynamical characteristics at different regimes of operation. In the testing phase, with a window of observation sequence (e.g., pressure time series), it is possible to find the likelihoods of the observed data sequence with respect to the pre-trained HMM. With a sliding-window calculation of the model likelihoods, an appropriate norm based on likelihood ratio has been chosen as the metric for detecting instabilities, which shows a monotonically increasing trend as the time-series signals approach limit cycle behavior through the transient mode of operation. This trend is consistent with the increasing fluctuation amplitudes of the signal during the transients,

and thus can be directly correlated to the overall growth rate of pressure oscillations (Hummel et al., 2017). It is also noted that data-driven methods, which have been studied for classification of unstable and stable modes in combustion systems, have largely focused on the usage of (statistically weak-sense stationary) stable or unstable time-series data (Gotoda et al., 2012; Nair and Sujith, 2014; Sarkar et al., 2016). The proposed method, in addition, is capable of handling non-stationary data such that the embedded information can be gainfully used for system identification. The results derived from experimental data have shown that it is possible to achieve good accuracy of detection even with a short window of time series (e.g., data over window sizes of about 10 ms corresponding to a sampling frequency of 8192 Hz), which matches with the time scale of TAI evolution. Such detection techniques are relevant for real-time monitoring and active control of TAI, where fast and computationally efficient detection/classification can provide appropriate lead-time to the actuators. From these perspectives, the major contributions of this paper are delineated below:

(a) Development of data-driven, HMM-based robust algorithms to facilitate near-real-time monitoring and active control of thermoacoustic instabilities from short-length time series of pressure oscillations.
(b) Experimental validation of the above algorithms on an electrically heated Rijke tube apparatus.

The laboratory apparatus and experimental procedure

The experimental data to validate the proposed concept have been generated from a laboratory-scale electrically heated Rijke tube apparatus as shown in Figure 1. It is well known that Rijke tubes possess some of the important characteristics of practical combustion systems like gas turbine combustors (for example, acoustically compact localized heat source). The simplicity of the experimentation and their capability of generating clean signals have made electrically heated Rijke tubes popular for investigations on fundamental aspects of thermoacoustic instabilities and their control (Gelbert et al., 2012). The apparatus comprises a 1.50 m long horizontal Rijke tube with an external cross-section of 0.1 m × 0.1 m and a wall thickness of approximately 6.35 mm. The inlet air flow is supplied by a compressor, which is prone to pressure fluctuations and is also expected to have moisture and other impurities. A Parker *P32E* series air filter-regulator is used to suppress the pressure fluctuations and to filter the impurities. The mean air flow is then controlled through a 0–1000 standard liters per minute (LPM) Alicat mass flow controller. The heating element in the Rijke tube is a square weave 40 × 40 nichrome wire mesh which is brazed to two copper strips on a machinable ceramic frame (Matveev, 2003) and is placed at about quarter length of the tube from the air input end (i.e., $x/L = 0.25$). The heating element is powered by a TDK Lambda programmable (0–8 V DC, 0–400 Amps) DC power source (Gopalakrishnan and Sujith, 2014). The horizontal arrangement of the tube allows an independent control of the flow rate and the heater power. Two damping chambers are provided at the two ends of the tube in order to ensure that the tube ends are maintained at pressure nodes under open-open boundary conditions. The damping

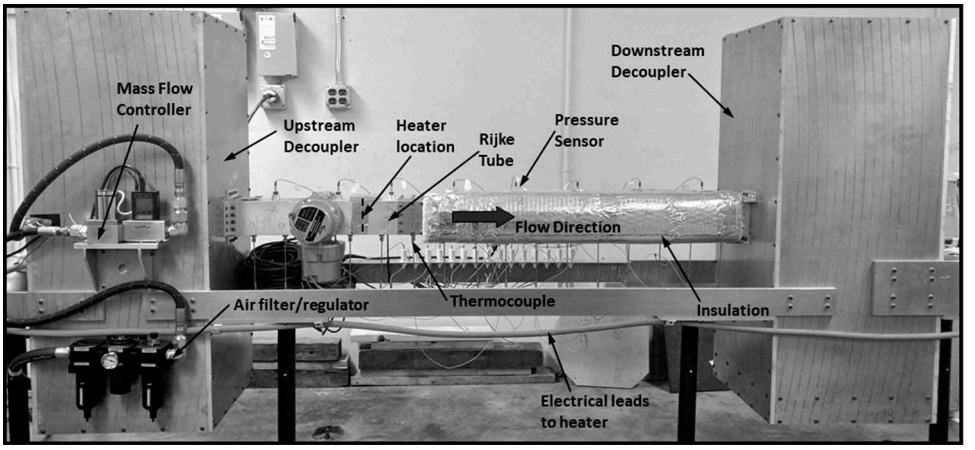

Figure 1. The Rijke tube experimental apparatus.

chambers also serve in decoupling the acoustics of the tube from those of the main air line. The chamber dimensions are 0.45 m × 0.45 m × 1.14 m. As a safety measure against the downstream half of the tube is insulated to reduce heat loss and to guard against any accidental physical contact with the hot metal surface.

Eight PCB-116B03 pressure sensors and fifteen K-type Omega thermocouple probes have been used for acquiring the acoustic and temperature data from the experiments. The first and the eighth pressure sensors are placed at a distance of 125 mm from the tube ends, while the distance between two consecutive sensors is approximately 180 mm. The sensors are powered through an 8-channel unity gain signal conditioner. The pressure sensors have a high sensitivity of 6 pC/psi and are coupled with in-line charge converters having an amplification of 100 mV/pC. The 13 out of the 15 thermocouple probes are placed downstream of the heater with an intermediate spacing of 90 mm, while the remaining two are placed upstream starting with a distance of approximately 63 mm from the upstream tube end. The thermocouple probes are capable of measurements up to 1360°C. All sensors are flush-mounted with the inner walls of the Rijke tube to reduce friction in air flow path. The sensor data acquisition and the voltage input to the programmable power supply unit are automated using DAQ devices from National Instruments (NI) in conjunction with NI LabVIEW 2016. The pressure sensor data is acquired through an NI-9205 (C Series Voltage Input Module) and the thermocouple data through an NI-9213 (C Series Temperature Input Module). The DC voltage supply is controlled through an NI-9264 (C Series Voltage Output Module).

The pressure sensor data are sampled at a rate of 8192 Hz and the acquired data are filtered with a 20th order Butterworth high-pass filter having a cutoff frequency of 40 Hz in order to eliminate low-frequency noises and acoustics from the damping chambers along with other environmental effects. To find the stability map of the system, steady state runs are performed after the tube is subjected to a warming up phase. After each experiment, a cool-off settling period is maintained to ensure similar steady-state initial temperature fields in the tube for each experiment. Maintaining similar initial temperatures ensure that the mean velocity of the sound waves in the air

remain approximately constant for each experiment, which in turn ensures that the fundamental frequency of the tube is kept constant.

Experiments have been conducted by varying the heater power input (E_{in}) and air flow rate (Q). For each operating condition, 10 s of sensor data have been recorded and the results are summarized in Figure 2, where unstable conditions are indicated by "×" and stable conditions by "o", the shaded boxes correspond to the unstable conditions with the higher dominant frequency in the vicinity of 131 Hz, and the emboldened box margins indicate operating conditions for which the pressure signature is depicted in Figure 3.

Two sets of initial temperatures have been explored in order to demonstrate the effect of changing the mean temperature on the stability characteristics. Two different regimes of instability have been observed based on the initial temperature profiles. When a lower initial mean temperature of around 27°C was maintained, a lower frequency mode of instability (~114 Hz) was observed to be excited for a range of flow rates marked with "×" in unshaded boxes in Figure 2. The shaded boxes indicate the conditions when the higher frequency unstable mode (~131 Hz) and its harmonics are excited with a higher initial mean temperature of about 75°C. These observations can be attributed to the increase in the speed of sound with the elevated mean temperature which changes the fundamental frequency from an analytically calculated value of 115 Hz to 127 Hz for an open-open tube, tallying closely with the experimentally procured peak frequencies. Figure 3 shows the representative plots of the fluctuating pressure amplitudes and their respective FFT for three different operating conditions marked as boldfaced boxes in Figure 2. The 131 Hz fundamental mode and its harmonics are excited with the power input of 1400 W at a flow rate of 162 LPM, which corresponds to a higher initial temperature profile, as discussed in the previous paragraph. The 114 Hz mode is excited at a lower power of 600 W and a flow rate of 112 LPM, with a lower initial temperature profile. The case with E_{in} = 1400 W, Q = 228 LPM has a stable behavior without any excited mode of limit cycle instability, which is also reflected in the significantly lower peak-to-peak amplitude of the fluctuating acoustic signal.

E_{in} (W) / Q (LPM)	61	72	82	92	102	112	122	132	142	152	162	172	182	191	200	210	219	228	237	246	255	264	273	281	290
2000	o	o	o	o	o	o	o	x	x	x	x	x	x	x	x	x	x	x	x	x	o	o	o	o	o
1800	o	o	o	o	o	o	o	x	x	x	x	x	x	x	x	x	x	x	x	x	o	o	o	o	o	o
1600	o	o	o	o	o	o	o	o	x	x	x	x	x	x	x	x	x	x	o	o	o	o	o	o	o	o
1400	o	o	o	o	o	o	o	o	x	x	x	x	x	x	x	x	o	o	o	o	o	o	o	o	o	o
1200	o	o	o	o	o	o	o	o	x	x	x	x	x	x	x	x	o	o	o	o	o	o	o	o	o	o
1000	o	o	o	o	o	o	o	o	x	x	x	x	x	x	o	o	o	o	o	o	o	o	o	o	o	o
800	o	x	x	x	x	x	x	x	x	x	o	o	o	o	o	o	o	o	o	o	o	o	o	o	o	o
600	o	x	x	x	x	x	x	x	o	o	o	o	o	o	o	o	o	o	o	o	o	o	o	o	o	o
400	o	x	x	x	x	x	o	o	o	o	o	o	o	o	o	o	o	o	o	o	o	o	o	o	o	o
200	o	o	o	o	o	o	o	o	o	o	o	o	o	o	o	o	o	o	o	o	o	o	o	o	o	o

Figure 2. Stability map of the system based on power input and air flow rate variations, where unstable conditions are indicated by "×" and stable conditions by "o". Shaded boxes correspond to the unstable conditions with the higher dominant frequency in the vicinity of 131 Hz. Emboldened box margins indicate operating conditions for which the pressure signature is depicted in Figure 3.

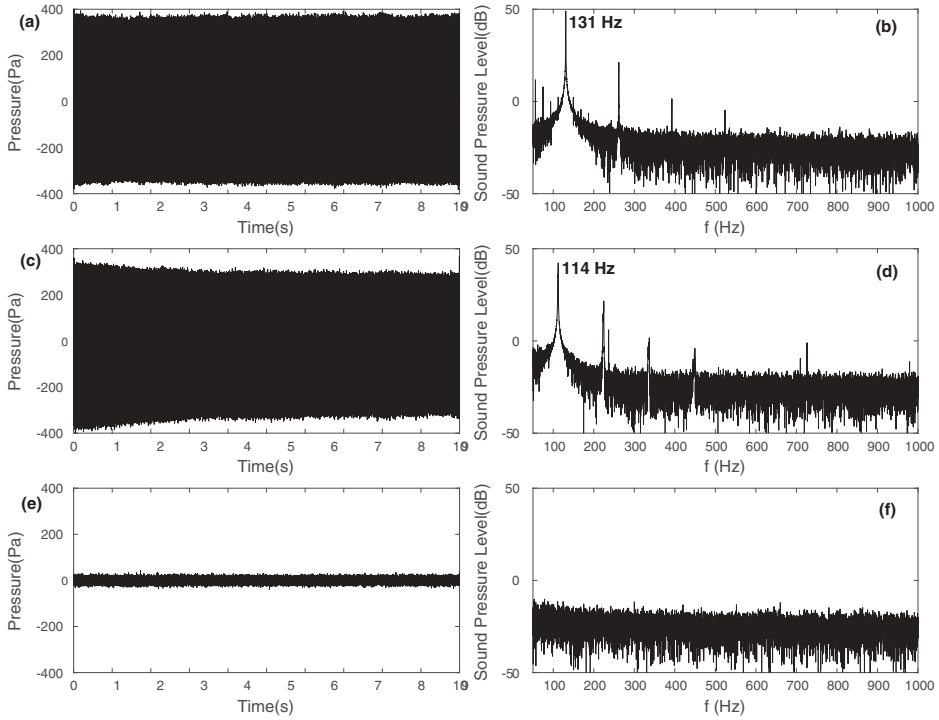

Figure 3. Representative plots of fluctuating pressure amplitudes (left) and their respective power spectral densities (right) at different operating conditions. (a) and (b): E_{in} = 1400 W, Q = 162 LPM. (c) and (d): E_{in} = 600 W, Q = 112 LPM. (e) and (f): E_{in} = 1400 W, Q = 228 LPM.

Mathematical background: hidden Markov modeling

This section briefly introduces the essential concepts of HMM, which form the building block for analyzing combustion dynamics as presented in this paper. Further details are available in Rabiner (1989), Murphy (2012), Bishop (2007), and Hajek (2015).

The concept of HMM has been widely used for representation of long-range dependencies between observations, where the underlying models are assumed to be probabilistic functions of the hidden states (Murphy, 2012). Considering a discrete-time representation of a sequence $\mathbf{Y} = \{y_1, y_2, \ldots, y_T\}$ of T continuous (i.e., real-valued) observations, and assuming a first-order Markov property (Bishop, 2007) over the observations, the joint probability density function of $\mathbf{Y}$ is obtained as:

$$p(\mathbf{Y}) = p(y_1) \prod_{t=1}^{T-1} p(y_{t+1}|y_t) \tag{1}$$

Although the above assumption has been widely used in practice, it may not be valid in many applications because of long-range correlations among the observations (Bishop, 2007; Murphy, 2012).

The HMM belongs to a class of doubly embedded stochastic processes, with a latent stochastic process of *hidden* state evolution. Although this evolution is not directly observed, it can be inferred by observing another stochastic process that produces the

sequence of observations (Rabiner and Juang, 1993), which captures the long-range dependencies among observations and enables the usage of HMMs as black-box density models on observation sequences. The major difference between the HMM and the standard Markov model is that the HMM does not assume the Markov property (i.e., conditionally dependence on the states and being independent of each other) for the observations themselves. Instead, the hidden state sequence $Z = \{z_1, z_2, \ldots, z_T\}$ are assumed to follow Markovian dynamics, i.e., given the current state z_t, the future state z_{t+1} is independent of all the states prior to time instant t. Figure 4 illustrates the idea with a Bayesian network model of a simple HMM. Following the convention of directed graphical models in the left hand plate of Figure 4, a shaded node z_i denotes a hidden variable, an unshaded (i.e., clear) node y_i denotes an observed variable and an arrow denotes conditional dependence. In the right hand plate of Figure 4, the arrows denote the transitions from state Z_i to Z_j with probability a_{ij}, where the states belong to a finite and discrete set $\mathcal{Q}$ and the cardinality $|\mathcal{Q}| = K$ is a positive integer.

To formalize the mathematical structure, let a string of observations $\{y_1, \ldots., y_T\}$ be assumed to be generated by a hidden state sequence $\{z_1, \ldots., z_T\}$. An HMM is then constructed as a triplet $\lambda = \{A, B, \pi\}$ (Rabiner, 1989), where:

(a) $A \stackrel{\Delta}{=} [a_{ij}]$ is the $K \times K$ state-transition probability matrix:

$$a_{ij} = p(z_{t+1} = q_j | z_t = q_i) \; : \; q_i, q_j \in \mathcal{Q}$$

where $\sum_j a_{ij} = 1 \; \forall i$.

(b) $B \stackrel{\Delta}{=} [b_j(y_t)]$ is the probability density of the observation given the state:

$$b_j(y_t) = p(y_t | z_t = q_j)$$

(c) $\pi \stackrel{\Delta}{=} [\pi_i]$ is the probability distribution of the initial state z_1: $\pi_i = p(z_1 = q_i)$, where π is a $1 \times K$ vector with $\sum_i \pi_i = 1$.

Following the above model λ, the corresponding joint probability distribution of states and observations has the form:

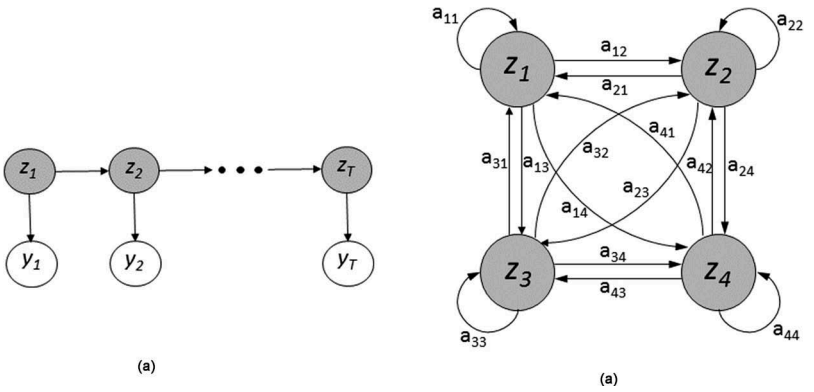

Figure 4. Left hand plate: Bayesian network model of an HMM showing conditional dependence of observations with hidden Markov states. Right hand plate: state transitions in a 4-state HMM (i.e., $K = 4$) .

$$p(\mathbf{Y},\mathbf{Z}) = p(z_{1:T})p(y_{1:T}|z_{1:T}) = \left[p(z_1)\prod_{t=1}^{T-1}p(z_{t+1}|z_t)\right]\left[\prod_{t=1}^{T}p(y_t|z_t)\right] \tag{2}$$

Here the HMM is assumed to have a continuous real-valued observation model, where the observations $\{y_1, ..., y_T\}$ are one-dimensional and their emission probability follows a Gaussian mixture model:

$$p(y_t|z_t = q_j, \lambda) = \sum_{\ell=1}^{M} c_{j\ell}\,\mathcal{N}(y_t, \mu_{j\ell}, \Sigma_{j\ell}) \tag{3}$$

where $\sum_{\ell=1}^{M} c_{j\ell} = 1$, $\forall j \in \{1, \ldots, K\}$; M is the number of Gaussian mixture components; and $\mathcal{N}(y_t, \mu_{j\ell}, \Sigma_{j\ell})$ represents Gaussian density function of y_t with mean $\mu_{j\ell}$ and covariance $\Sigma_{j\ell}$ associated with state q_j and mixture component ℓ.

Two main model parameters are, therefore, the number of hidden states (K) and the number of mixture components (M), which need to be optimally selected in the context of HMMs (Celeux and Durand, 2008; Rydén, 1995); and AIC/BIC based techniques (Akaike, 1974; Schwarz, 1978) are most commonly used to select the optimal model parameters that maximize the likelihood of the data and minimize the model complexity, thereby balancing the goodness of fit against model complexity to alleviate data overfitting. This paper has adopted the BIC model selection function for choosing the parameters K and M. Thus, the model learning problem is to find the optimal set of parameters for $\lambda = \{A, B, \pi\}$ in order to maximize $P(\mathbf{Y}|\lambda)$. It is achieved through a commonly used iterative procedure called *Baum-Welch Algorithm* which is an application of Expectation-Maximization method for inferring HMM parameters (Rabiner, 1989).

Now, given an observation sequence $\mathbf{Y} = \{y_1, y_2, \ldots, y_T\}$ and an HMM model λ, the problem at hand is to find the probability of the entire observation sequence so that it can be associated with the most likely model from a bank of pre-trained HMM models. This is expressed as:

$$p(\mathbf{Y}|\lambda) = \sum_{Z} p(\mathbf{Y}|\mathbf{Z},\lambda)p(\mathbf{Z}|\lambda) = \sum_{z_1,z_2,,z_T} \pi_{z_1} b_{z_1}(y_1) a_{z_1 z_2} b_{z_2}(y_2) \ldots a_{z_{T-1} z_T} b_{z_T}(y_T) \tag{4}$$

The calculation of $p(\mathbf{Y}|\lambda)$ according to the direct definition as in Eq. (4) has computational complexity in the order of $(2TK^T)$ which may become intractable for even small values of K and T. For numerical efficiency, the well-known *Forward Procedure* is used, which reduces computational complexity to the order of (K^2T). The relevant algorithms are briefly discussed in the following subsections.

A. The forward procedure

The forward variable $\alpha_t(i)$, defined as $\alpha_t(i) \stackrel{\Delta}{=} p(y_1, y_2, \ldots, y_t, z_t = q_i|\lambda)$ is the probability that, provided the model λ is being followed, the partial observation sequence $\{y_1, y_2, \ldots, y_t\}, 1 \leq t < T$ until time t ends with the state of the system being q_i at time t. This can be solved inductively as follows:

$$1.\ \text{Initialization step}: \quad \alpha_1(i) = \pi_i b_i(y_1), \quad 1 \le i \le \mathrm{K} \tag{5}$$

$$2.\ \text{Induction step}: \quad \alpha_{t+1}(j) = \left[\sum_{i=1}^{K} \alpha_t(i) a_{ij}\right] b_j(y_{t+1}), \quad 1 \le \mathrm{t} \le \mathrm{T}-1, \quad 1 \le j \le \mathrm{K} \tag{6}$$

$$3.\ \text{Termination step}: \quad p(\mathbf{Y}|\lambda) = \sum_{i=1}^{K} \alpha_T(i) \tag{7}$$

where the parameters T and K are the same as defined earlier.

B. The backward procedure

The backward variable $\beta_t(i)$, defined as $\beta_t(i) \triangleq p(y_{t+1}, y_{t+2}, \ldots, y_T | z_t = q_i, \lambda)$, is the probability of the partial observation sequence $\{y_{t+1}, y_{t+2}, \ldots, y_T\}$ from t + 1 till the end, provided that the state at time t is q_i and the model followed is λ. This can be solved inductively as follows:

$$1.\ \text{Initialization step}: \quad \beta_T(i) = 1, \quad 1 \le i \le \mathrm{K} \tag{8}$$

$$2.\ \text{Induction step}: \quad \beta_t(i) = \left[\sum_{j=1}^{K} a_{ij} b_j(y_{t+1}) \beta_{t+1}(j)\right], \quad \mathrm{t} = \mathrm{T}-1, \mathrm{T}-2, \ldots, 1, \quad 1 \le i \le \mathrm{K} \tag{9}$$

where the parameters T and K are the same as defined earlier.

C. Model learning: Baum-Welch algorithm

The model learning problem requires the estimation of the model parameters $\lambda = \{A, B, \pi\}$ so as to maximize the likelihood $p(\mathbf{Y}|\lambda)$. Baum-Welch algorithm is a recursive estimation procedure of the HMM parameters. Given the model and the observation sequence, the intermediate variables ξ and γ are defined, for $1 \le i \le K$, $1 \le j \le K$ and $1 \le t \le T$, as:

$$\xi_t(i,j) \triangleq P(z_t = q_i, z_{t+1} = q_j | \mathbf{Y}, \lambda) \tag{10}$$

$$\gamma_t(i) \triangleq p(z_t = q_i | \mathbf{Y}, \lambda) \tag{11}$$

The variables γ_t and $\xi_t(i,j)$ are expressed in terms of the forward and backward variables α_t and β_t, defined earlier as:

$$\begin{aligned} \gamma_t(i) &= \frac{\alpha_t(i)\beta_t(i)}{p(\mathbf{Y}|\lambda)} = \frac{\alpha_t(i)\beta_t(i)}{\sum_{i=1}^{K} \alpha_t(i)\beta_t(i)}, \\ \xi_t(i,j) &= \frac{\alpha_t(i) a_{ij} b_j(y_{t+1}) \beta_{t+1}(j)}{\sum_{i=1}^{K} \sum_{j=1}^{K} \alpha_t(i) a_{ij} b_j(y_{t+1}) \beta_{t+1}(j)} \end{aligned} \tag{12}$$

Using the above relations, and the fact that $\gamma_t(i) = \sum_{j=1}^{K} \xi_t(i,j)$, it is possible to estimate $\{A, B, \pi\}$ as:

$$\hat{\pi}_i = \gamma_1(i) \tag{13}$$

$$\hat{a}_{ij} = \frac{\sum_{t=1}^{T-1} \xi_t(i,j)}{\sum_{t=1}^{T-1} \gamma_t(i)} \tag{14}$$

$$\hat{c}_{jk} = \frac{\sum_{t=1}^{T} \tilde{\gamma}_t(j,k)}{\sum_{t=1}^{T} \sum_{k=1}^{M} \tilde{\gamma}_t(j,k)} \tag{15}$$

$$\hat{\mu}_{jk} = \frac{\sum_{t=1}^{T} \tilde{\gamma}_t(j,k).y_t}{\sum_{t=1}^{T} \tilde{\gamma}_t(j,k)} \tag{16}$$

$$\hat{\Sigma}_{jk} = \frac{\sum_{t=1}^{T} \tilde{\gamma}_t(j,k).(y_t - \mu_{jk})^2}{\sum_{t=1}^{T} \tilde{\gamma}_t(j,k)} \tag{17}$$

where $\tilde{\gamma}_t(j,k)$ is the probability of being in state q_j at time t with the k^{th} mixture component. That is,

$$\tilde{\gamma}_t(j,k) = \left[\frac{\alpha_t(j)\beta_t(j)}{\sum_{j=1}^{N} \alpha_t(j)\beta_t(j)}\right]\left[\frac{c_{jk}\mathcal{N}(y_t, \mu_{jk}, \Sigma_{jk})}{\sum_{k=1}^{M} c_{jk}\mathcal{N}(y_t, \mu_{jk}, \Sigma_{jk})}\right] \tag{18}$$

It is noted that the term $\tilde{\gamma}_t(j,k)$ generalizes to $\gamma_t(j)$ in case of a single-component Gaussian density (i.e., $M = 1$) or a (discrete) probability mass function.

The model $\hat{\lambda} = \{\hat{A}, \hat{B}, \hat{\pi}\}$ can be recursively estimated until it converges to a local maxima of the likelihood function $p(\mathbf{Y}|\lambda^*)$, where λ^* is the maximum likelihood estimate of the HMM. More details on the Baum-Welch algorithm and forward-backward algorithm are available in (Hajek, 2015; Rabiner, 1989).

Technical approach

This section presents the technical approach for autonomous detection of thermoacoustic instabilities (TAI) based on time series of pressure oscillations, where regime identification is an important and challenging task. In this context, Rigas et al. (2016) have demonstrated on a Rijke tube apparatus, similar to the apparatus described earlier, that a transition can be made from a stable fixed point to a limit-cycle mode of operation if the heater power is increased beyond the Hopf bifurcation point (Thompson and Stewart, 1986). Since thermoacoustic instabilities are understood to be an outcome of subcritical Hopf bifurcations, it is imperative to devise efficient detection methodologies that can identify the shift in operational regime during an early transient period, before it reaches a limit-cycle behavior. This is the rationale for having a rich source of data that will be capable of demonstrating the transient behavior of the pressure time series as the combustion system passes through the bifurcation point. The following procedure, similar to the one demonstrated by Rigas et al. (2016), has been adopted in this paper:

(a) The experimental apparatus is heated to a steady state with the primary heater power input (E_{in}) $\approx$ 200 W.
(b) Then, the power input is abruptly increased to a higher value that showed limit cycle behavior as depicted in the stability chart in Figure 2.
(c) For each experiment, the air flow rate (Q) has been set at a constant value, and a series of experiments have been conducted with Q ranging from 130 LPM to 250 LPM at increments of 20 LPM.
(d) Pressure data have been recorded using the acoustic sensors over a 30-s window at a sampling rate of 8192 Hz.

During each experiment, within the aforesaid 30-s window, the transition data from the stable regime to an unstable (limit-cycle) regime (which occurs through the bifurcation point) have been collected from the pressure sensors. The ensemble of collected data contains unsteady pressure signals for several experimental conditions having respective responses with different amplitudes of limit-cycle oscillations. This dataset provides a rich source of information for the three regimes, namely, stable, transient, and unstable (limit-cycle), which is used for learning generative statistical models of these three operational regimes. It is noted that the SNR may vary with individual sensors, as seen in the typical profiles of pressure signals in Figure 5. For the data profile of a pressure sensor (immediately downstream of the heater) in Figure 5(a), the power input is abruptly increased to 1800 W at time ~17 s from the initial 200 W preheated condition and the air flow rate is kept constant at 210 LPM; Figure 5(b) shows qualitatively similar responses from another pressure sensor (further downstream of the heater), where the power input has been abruptly increased to 2000 W at time ~17 s from the initial 200 W preheated condition and the air flow rate is kept constant at 250 LPM. The SNR in the data collected from these two sensors is also different due to their proximities from the heater, as seen in the textures of the time series in Figure 5(a) as compared to those in Figure 5(b).

Having the domain knowledge of stable, transient and the limit-cycle operational regimes, the task at hand is to train three HMMs: λ_i, for $i \in \{1, 2, 3\}$, where λ_1 corresponds to the stable regime of operation, λ_2 corresponds to the transient growth regime, and λ_3 corresponds to the unstable (limit-cycle) regime. This task accomplishes a generative modeling of the system dynamics based on the domain knowledge procured by the

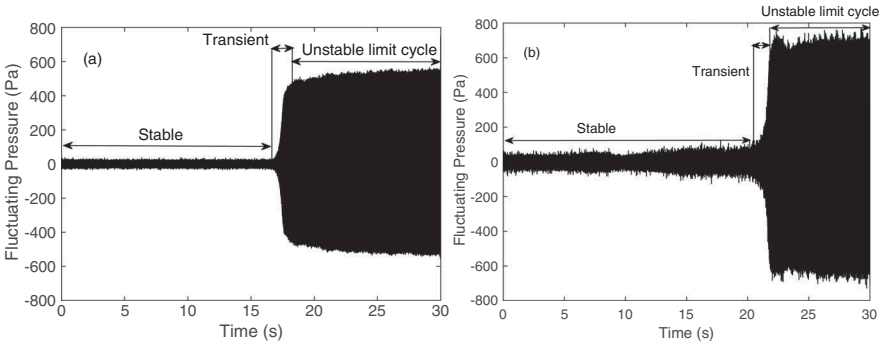

Figure 5. Unsteady pressure signals showing the transience from stable fixed point to limit cycle through bifurcation. (a) E_{in} abruptly increased to 1800 W with $Q = 210$ LPM .(b) E_{in} abruptly increased to 2000 W keeping $Q = 250$ LPM.

experiments. It is noted that although the experiments have been conducted to encompass a wide range of operating conditions and power input profiles to the heating unit, it is infeasible to conduct experiments under all different operational conditions that a real-life combustor may undergo. Nevertheless, the HMMs are intended to learn the trend in the data that are used for training the models. So, with a sufficiently rich set of training data procured from different regimes, HMMs can be used to encapsulate the dynamics of the behavioral characteristics of the combustion system in different regimes. Such a "context-based" learning makes sense in this respect because, for example, the signature of the pressure signals in the unstable (limit-cycle) regime is expected to have a deterministic periodic nature, which is much different from the noisy or chaotic nature generally exhibited in the stable regime. Learning generative models based on ensembles of data from these three operational regimes ensures that the underlying model is robust to uncertainties such as variations in operational conditions and sensor noise even for a single operational regime.

Test data of pressure time series have been used with the pre-trained models for early detection of thermoacoustic instabilities (TAI). Given a window of time series $\{y_1, ..., y_T\}$, the log-likelihood L_k and the log-likelihood ratio (LLR) $[L_k - L_1]$ are obtained as:

$$(L_k \stackrel{\Delta}{=} \log p(y_{1:T})|\lambda_k) \text{ for } k = 1, 2, 3) \Rightarrow ([L_k - L_1] = \log\left[\frac{(p(y_{1:T})|\lambda_k)}{(p(y_{1:T})|\lambda_1)}\right] \text{ for } k = 2, 3) \tag{19}$$

where $(p(y_{1:T})|\lambda_k)$ denotes the probability that the observed pressure time series is generated by the HMM λ_k, for $k \in \{1, 2, 3\}$. The rationale here is that as the system deviates from the stable regime and the transient growth tends toward limit-cycle instabilities, the signature of pressure oscillations would have a higher probability to be generated from either λ_2 or λ_3 than from λ_1, which is reflected from the LLR $[L_k - L_1]$ in Eq. (19) being positive for $k = 2, 3$.

Focusing on short-length windows of time series in this paper to address real-time monitoring and active control, early detection of TAI would provide appropriate lead-time for the actuators to implement the control action. The procedure involved in the analysis is described as follows:

(a) The window size is chosen for a time scale of ~10–100 ms, because the bifurcation mode of instability evolution occurs in the time scale of milliseconds. Hence, online detection of TAI with such a length of time window should be able to provide appropriate lead-time to the actuators to implement the control actions for suppressing the pressure oscillation.
(b) Time-series data in subsequent batches of the chosen window length is used to calculate $(p(y_{1:T})|\lambda_k)$, for k = 1, 2 and 3.
(c) The LLR in Eq. (19) is chosen as the norm for detecting instability onset. The ratio is calculated for each batch of data being analyzed and condition monitoring is performed based on the evolution of the norm over batches of time-series samples.

Results and discussions

This section presents the results of experimental validation of the proposed HMM-based method on the Rijke tube apparatus and compares these results with the results of similar data-driven techniques on the same data sets for estimating the growth rates of thermo-acoustically unstable systems.

A. Detection of early onset of instabilities

This subsection presents the results for detecting instabilities during the transient regime. The dataset used for this purpose comprises an ensemble of 145 sets of pressure time series with 30-s duration similar to those depicted in Figure 5. This entire dataset has been randomly divided into training and testing sets in the ratio 80:20. The training data are first used to train the three HMMs, λ_1, λ_2 and λ_3. The test data for detection of TAI are chosen to be truncated just before the onset of unstable (limit-cycle) regime, and the performance of the classifier for instability detection is based on successful detection of the onset of short-duration transients even before the limit cycle begins. This requirement poses a stringent condition on the classifier to perform early detection of instability evolution with dynamic sensor data. The idea here is that the underlying algorithm should be able to detect a divergence from the stable regime (i.e., nominal operation) well within the transient regime sufficiently before the unstable (limit-cycle) regime begins; this is necessary because a major failure can be triggered by structural resonance in the unstable regime when it might be too late to exercise control actions. The testing phase involves calculating the LLR in Eq. (19)) for classifying each data window. In the framework of Bayesian binary hypothesis testing, the proposed algorithm classifies each pressure time-series window into either *stable* (Class A) or *unstable* (Class B) based on the following LLR test (see also Eq. (19)):

$$[L_k - L_1] = \log\left[\frac{(p(y_{1:T})|\lambda_k)}{(p(y_{1:T})|\lambda_1)}\right] = \log[(p(y_{1:T})\lambda_k)] - \log[(p(y_{1:T})|\lambda_1)] \underset{\mathrm{G}}{\overset{\mathrm{H}}{\gtrless}} \tau \text{ for } k = 2 \text{ or } 3 \tag{20}$$

where τ is a user-specified threshold (Poor, 2013). A commonly used criterion to choose τ is the receiver operating characteristic (ROC) curve that is obtained by varying τ to provide a trade-off between the probability of successful detection ($p_D \overset{\Delta}{=} p[\text{Decided Class} = H|\text{True Class} = H]$) and the probability of false alarms ($p_F \overset{\Delta}{=} p[\text{Decided Class} = H|\text{True Class} = G]$).

Figure 6 shows a family of ROC curves for the proposed HMM-based detection algorithm using different window sizes of data, with the likelihood ratio chosen as $\log\left[\frac{(p(y_{1:T})|\lambda_2)}{(p(y_{1:T})|\lambda_1)}\right]$ (i.e., the probability that each observed sequence belongs to the transient class as compared with the probability of belonging to the stable class), abbreviated as $[L_2 - L_1]$ henceforth. Similar ROC curves are obtained when the likelihood is compared with respect to the unstable and stable classes, i.e., $\log\left[\frac{(p(y_{1:T})|\lambda_3)}{(p(y_{1:T})|\lambda_1)}\right]$ (abbreviated as $[L_3 - L_1]$) is used as the LLR. Due to the fact that data textures in the transient and unstable (limit-cycle) regimes are significantly different from those in the stable regime, LLRs generated

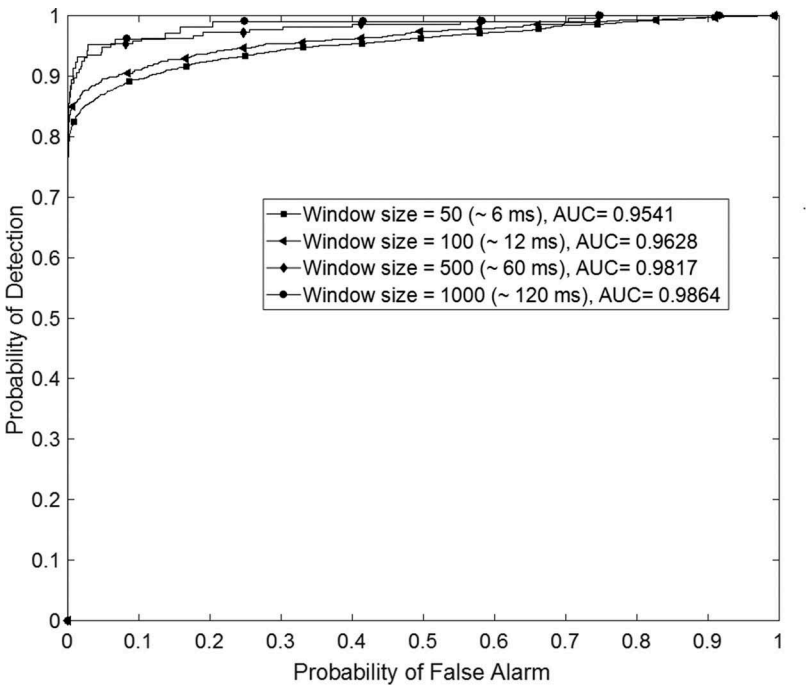

Figure 6. ROC curves for the proposed method with different window sizes of sensor time series.

by these two methods may be largely similar . Therefore, either $[L_2 - L_1]$ or $[L_3 - L_1]$ can be used as the classifier.

Window sizes of 50, 100, 500 and 1000 have been chosen for the plots in Figure 6, which corresponds to time scales in the order of milliseconds considering the sampling frequency of 8192 Hz. For example, a window size of 50 corresponds to a classifier decision taken after approximately every 6 ms. A commonly used method for comparing the performance of different classifiers is comparison of the area under the curve (AUC) of ROC for each classifier (Fawcett, 2006). Higher AUC is generally associated with a better overall performance of a classifier. As depicted in Figure 6, the AUC increases from 0.9541 to 0.9864 as the window size is increased from 50 to 1000, with progressively higher detection rates at specified false alarm rates. The rationale is that the classifier is expected to perform better with respect to larger lengths of observation sequences. It is worth reiterating that the anomalous class detected by the classifier in Figure 6 belongs to the transient phase of pressure time series, and hence, the high classification accuracy even with approximately 6–60 ms long data makes the proposed HMM-based classification scheme a promising candidate for TAI detection in an early part of the transient regime.

The trend in the variations of the LLR is now investigated as the time series passes through the transient regime. For demonstration purposes, the pressure signature recorded by the downstream sensor nearest to the heater has been chosen for the

experimental condition of increasing the heater power input abruptly to 2000 W while maintaining the flow rate at 250 LPM (see Figure 5(b)).

The testing data are analyzed according to batches of a chosen window length of 100 samples. Since the objective is early detection of TAI, the batches are continually analyzed for the entire time series until the limit-cycle instability is reached. Figure 7 shows the evolution of the LLR $[L_2 - L_1]$ (plotted with squares on solid line) as the sensor data are analyzed in batches of data length 100. The pressure time-series data are plotted by downsampling the actual time-series data by 100, because each successive log-likelihood calculation involves 100 pressure observation data. The vertical dashed line in Figure 7 indicates the separation between the stable and transient regimes. The onset of instabilities occurs after about 1700th sample, which corresponds to ~20 s in the actual time scale. It is noted that the associated LLR also changes abruptly from approximately zero value before the 1700th time sample to a very high positive value in the order of $\sim 10^4$, showing a very high sensitivity to the divergence of the pressure profile characteristics from the stable regime to the transient regime. In addition, the monotonicity in the increase of LLR is correlated to the degree of instability of pressure oscillations, which justifies its potential use as an index for measure of instabilities. This shows that the pre-trained HMMs are able to promptly distinguish the onset of transient growth from the stable regime early in the transient regime. The high sensitivity of the proposed detection method is attributed to the non-deterministic algebraic structure of HMMs along with its trained observation emission distribution, which results in a very good discriminative performance even with short lengths of observation.

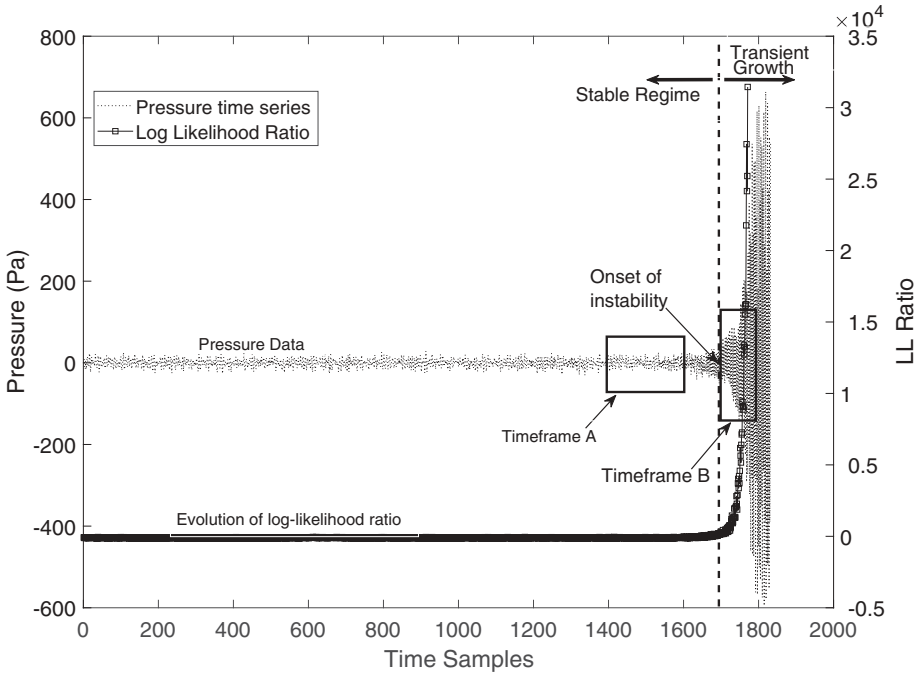

Figure 7. Evolution of LLR $[L_2 - L_1]$ (see Eq. (19)) with the pressure time-series data.

B. Regime detection

More insight is obtained from Figure 7 by analyzing the variations of the likelihoods with respect to λ_1, λ_2 and λ_3 in Timeframe A (1400–1600 samples) in the stable regime and Timeframe B (1600–1800 samples) in an early part of the transient regime. This is reflected in Figure 8 from the highest relative likelihood L_1 of the data corresponding to λ_1 (downfacing solid triangles), as compared with likelihoods L_2 and L_3 with respect to λ_2 (solid squares) and λ_3 (hollow circles), respectively. λ_3 has the lowest likelihood among the three, which can be traced back to the fact that λ_3 has been trained with data belonging to the unstable (limit-cycle) regime, the deterministic and periodic nature of which is quite different from the chaotic nature of stable regime data.

Figure 9 shows the evolution of the three likelihoods in Timeframe B of Figure 7 which spans from 1600 to 1800 time samples – the region of early transience from stable to unstable behavior. It is seen that the likelihood of the data belonging to the stable model λ_1 sharply drops as soon as the transience sets in, and this results in the sharp increase in the value of the LLR $[L_2 - L_1]$ as depicted in Figure 7. The respective variations in L_2 and L_3 are conspicuously observed in the inset of Figure 9. It is seen that L_2 dominates L_3 for the bulk of the Timeframe B, except at the very end when limit cycle behavior sets in, which causes L_3 to dominate L_2. Although both L_3 and L_2 should be able to distinguish the occurrence of anomalous behavior from L_1, the LLR $[L_2 - L_1]$ is expected to be more discriminative than the LLR $[L_3 - L_1]$ for transient regime detection.

From the perspective of regime classification, the HMMs exhibit a potential to discriminate between the transient and unstable (limit-cycle) data with respect to the pressure time-series signals. Figure 10 shows the evolution of L_2 and L_3 as the time series

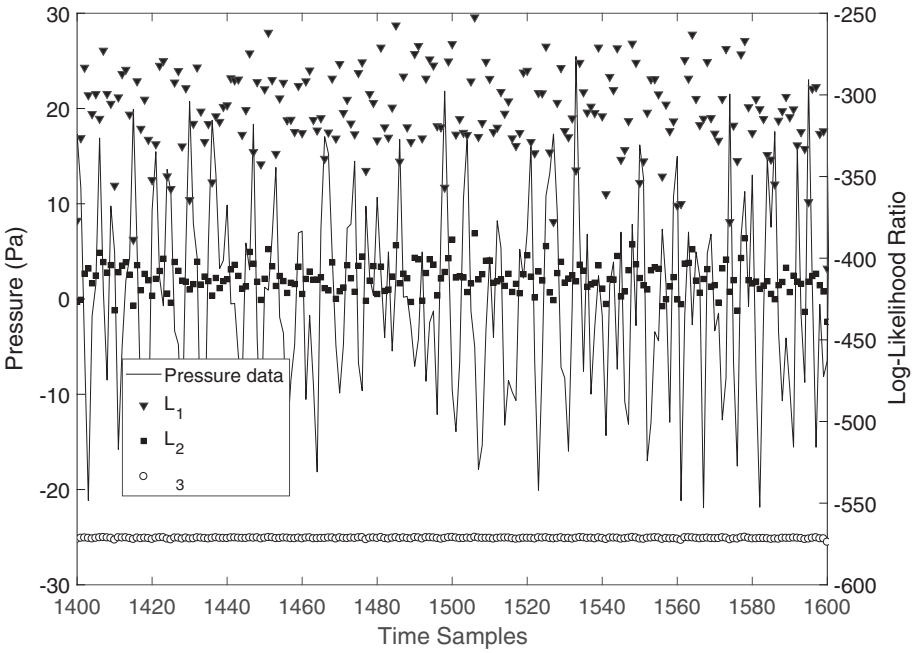

Figure 8. Log-likelihoods L_1, L_2 and L_3 (see Eq. (19)) with pressure samples in Timeframe A of Figure 7.

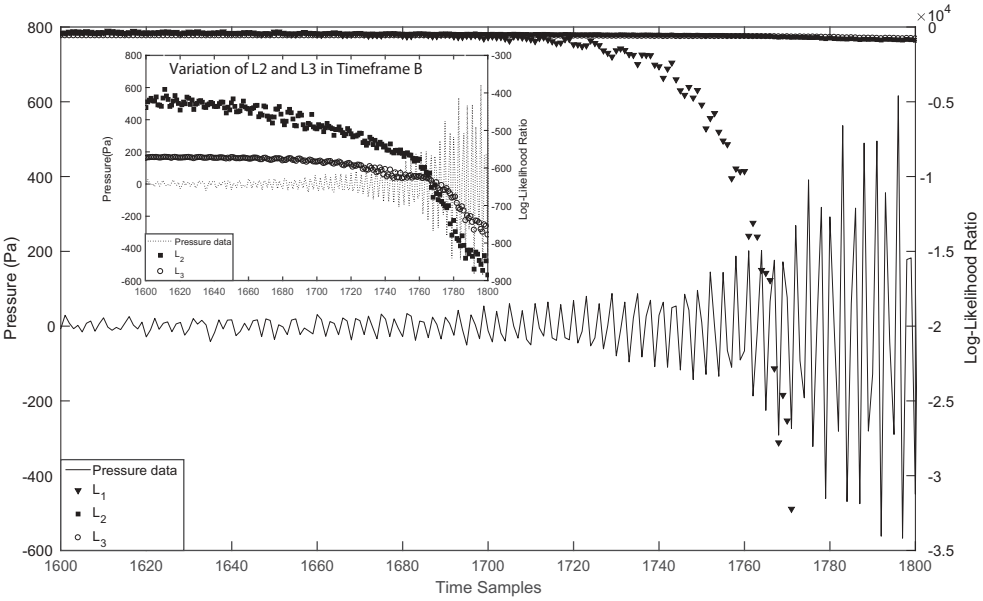

Figure 9. Log-likelihoods L_1, L_2 and L_3 (see Eq. (19)) with pressure samples in Timeframe B of Figure 7. The inset shows explicitly the variations of the log-likelihoods L_2 and L_3 within this timeframe.

passes from transient to unstable (limit-cycle) regime. It is seen that L_3 starts dominating L_2 as the unstable (limit-cycle) regime is approached, showing that the models have satisfactorily captured the dynamics of the system during the different regimes. So, for regime detection purposes, the information from the ROC curves (Figure 6) can be used to choose a particular threshold τ corresponding to the trade-off between the detection rate required by the user and the allowable false alarm in detection. The problem of regime detection is challenging because the classifier has to decide which of the three pre-trained regimes does a short data history belong to. Table 1 presents the regime detection accuracies, where the threshold τ has been chosen using the ROC of a classifier with $[L_3 - L_1]$ as the LLR with window size = 100; here τ has been chosen to correspond to about 92% detection rate with 10% allowable false alarm from the ROC curve.

The test data samples consist of 1000 random samples from each of the three regimes, which were classified using the chosen threshold of $[L_3 - L_1]$. The limit cycle unstable regime was distinguished from the transient growth regime by employing the LLR $[L_3 - L_2]$. It is interesting to note that the classifier designed for detecting instabilities in the transient regime is able to detect the unstable (limit-cycle) regime with 100% accuracy, implying that the detection algorithm is almost always sure to distinguish limit cycle data from the other two regimes. The superior performance in detecting unstable (limit-cycle) data is possibly due to its deterministic periodic nature. However, the presence of transience in the data makes its detection even more difficult and the method discussed in this paper can serve as a unified framework for this purpose.

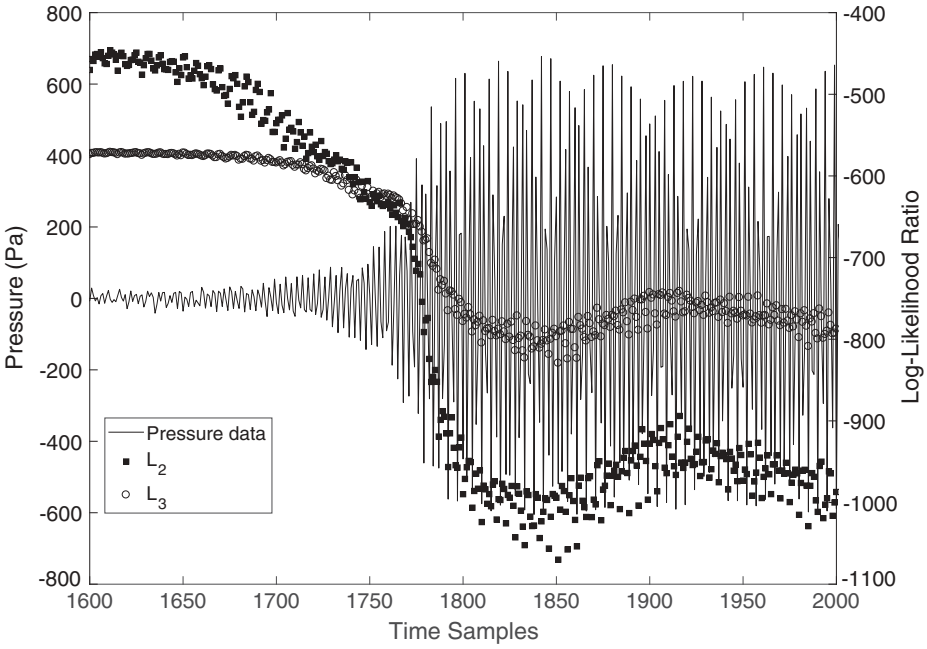

Figure 10. Log-likelihoods L_2 and L_3 (see Eq. (19)) with samples from transient to limit cycle regimes.

Table 1. Classification accuracy of the three regimes.

Stable regime	Transient regime	Unstable regime
90%	91%	100%

C. Comparison with growth rate measurement techniques

Information about the growth rates of linearly unstable systems has been shown to be useful for the design of robust controllers (Noiray and Schuermans, 2012). In fact, for real-time monitoring and active control of thermoacoustic instabilities, the growth rate information can be used to detect the onset of unstable modes. However, it is difficult to characterize the growth rate from an experimental point of view, as discussed by Moeck et al. (2007). An unstable combustion system generally exhibits an abrupt change from a stable regime to an unstable (limit-cycle) regime through a bifurcation, thereby posing serious challenges for data-driven growth rate extraction techniques to detect the growing trend in the data in that short period. Recently, Rigas et al. (2016) and Jamieson et al. (2017) have reported growth and decay rate measurements using transient acoustic time-series data from an electrically heated Rijke tube, similar to the apparatus used in the current paper . Their method is based on extracting clean regions of linear growth and decay from the Hilbert envelope of the time-series signal, and measuring the growth rate by a linear fit in the identified region. The application of this method to the current data is first reported and then certain issues are discussed related to the data length requirements.

The extraction of growth rate is based on the assumption that the combustion dynamics are governed by a single thermoacoustic mode, which is the dominant frequency of the self-excited oscillations (Lieuwen, 2003). Under this single mode approximation, the calculated growth rate

is essentially that of the dominant mode (ω) of the system (Boujo et al., 2016), which is around 130 Hz for the data analyzed in this section. To implement this concept, the time-series data from the Rijke tube apparatus have been filtered using a 20th order bandpass Butterworth IIR filter with lower 3-dB frequency of 120 Hz and higher 3-dB frequency of 140 Hz, in conjunction with a phase equalizing filter for preventing phase distortion in the filtered signal. This helps in reducing the noise and extracting clean regions of linear growth, which can then be identified by thresholding on the Hilbert amplitude to separate the approximately linear region between the noise floor and the nonlinearly dominated regions.

Figure 11 shows the evolution of the Hilbert envelope as a function of data length for the case when the heater power was increased abruptly to 1400 W with the air flow rate kept constant at 170 LPM. It can be seen in Figure 11(b) that it is possible to define upper and lower thresholds on the Hilbert amplitude to formulate a linear fit for extracting the linear growth rate as $\sigma_r = \frac{d(log(Amplitude))}{dt}$ when the Hilbert transform is performed on the complete data, as reported by Rigas et al. (2016). In Figure 11(c) the time-series data have been truncated to choose 1000 samples from the 18.5-s mark around which the system starts exhibiting transient growth. Since this sample window contains data from the transient regime, it should be associated with a positive linear growth rate of the dominant mode.

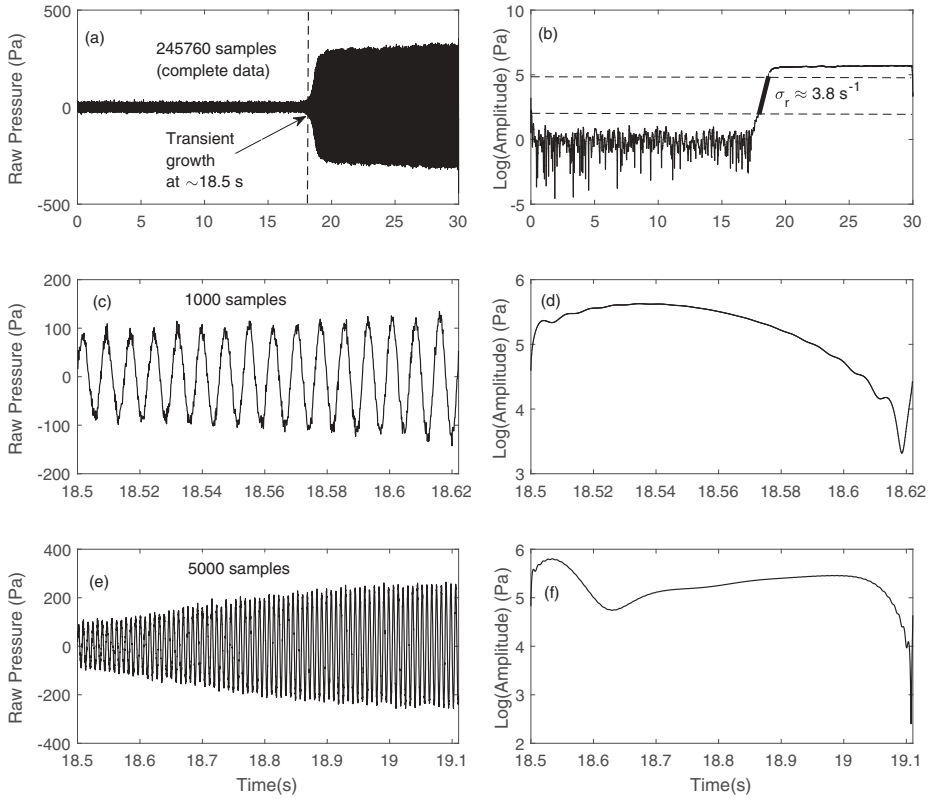

Figure 11. Hilbert envelope calculated from the pressure time-series data. (a), (c) and (e): Complete pressure data from 0 to 30 s (245,760 samples), from 18.5 to 18.62 s (1000 samples), from 18.5 to 19.1 s (5000 samples), respectively. (b), (d) and (f): Evolution of Hilbert envelope for cases (a), (c) and (e), respectively. The linear fit for calculating growth rate is shown as a bold line in (b).

The Hilbert envelope evolution in Figure 11(d) does not involve a similar linearly growing region from which the growth rate can be extracted. This is possibly because the envelope evolves slowly, and hence it requires more data. As seen in Figure 11(f), even when the data length was increased to 5000 samples from the 18.5-s mark, the Hilbert envelope does not show a conspicuous region of growth that can be described by a linear fit. Hence, although this technique can be used as an offline method to calculate the growth rate for different operating conditions, it is limited in its applicability as an online detection tool for extracting the growth rate of a dynamically evolving unstable thermoacoustic system. Moreover, the amplitude thresholds for the regions of noise floor and nonlinearity are expected to vary across different time samples, and would most likely be a strong function of the operating conditions and varying SNR of the sensors from which the samples are generated.

With the LLRs of the HMMs, one may classify short-length time windows in the transient regime, as was discussed earlier. For the time series with 1000 samples in Figure 11(c), $[L_2 - L_1] = 1.4303 \times 10^4$ (see Eq. (19)), and for the one with 5000 samples (Figure 11(e)), $[L_2 - L_1] = 44.814 \times 10^4$. Both the values are well above 0, implying that the data samples are far from the stable regime. If a sample size of 1000 can be afforded, a windowed likelihood calculation can be performed to find the trend in variation of the likelihood ratio, which would reflect the rate of growth in the time sample. Figure 12 shows the comparison between LLR variations using 1000 samples and the growth rate calculation using the complete dataset. Two cases have been investigated, Case 1 in which the power input has been increased to 1400 W keeping the flow rate constant at 170 LPM, and Case 2 in which the power input has been increased to 2000 W with the flow rate kept fixed at 230 LPM. Figure 12(a) shows the growth rates calculated using the complete time series of 30 s, with solid line representing Case 1 and dotted line representing Case 2 that has a higher growth rate of 4.4 s^{-1} as compared to 3.8 s^{-1} in Case 1. This is reflected in the likelihood ratio plot in Figure 12(b), where $[L_2 - L_1]$ has been calculated using a window size of 100 samples on a time-series sample of 1000 data points chosen from the inception of transient growth in both the cases. Case 2 (dotted line with triangles) in Figure 12(b) shows a progressively increasing rate of higher relative likelihood of λ_2 with respect to λ_1, which is consistent with the information obtained from the growth rate calculations. Since the likelihood ratio can be used to conclude the higher rate of growth using a much shorter time series from the early transient period, it can potentially be applicable to early detection of the rate of transient growth in the unstable regime.

D. Comparison of computational complexity with other data-driven techniques

To the best of the authors' knowledge, the current paper is the first reported work that aims to detect the growth of instabilities from non-stationary time-series data using a real-time data-driven approach. Most of the research reported in the combustion literature have proposed different data-driven tools for predicting precursors to instabilities from stationary time-series data, for example, steady-state pressure time series obtained as a function of equivalence ratio. Sarkar et al. (2016) have reported computational complexity of different data-driven methods for prediction of thermoacoustic instabilities using stationary time-series data. Nair and Sujith (2014) have correlated loss of multifractality with the onset of instability in the acoustic fluctuations by computing generalized Hurst exponents. Gotoda et al. (2012) have studied variations in the minimum of normalized permutation entropy as a function of equivalence

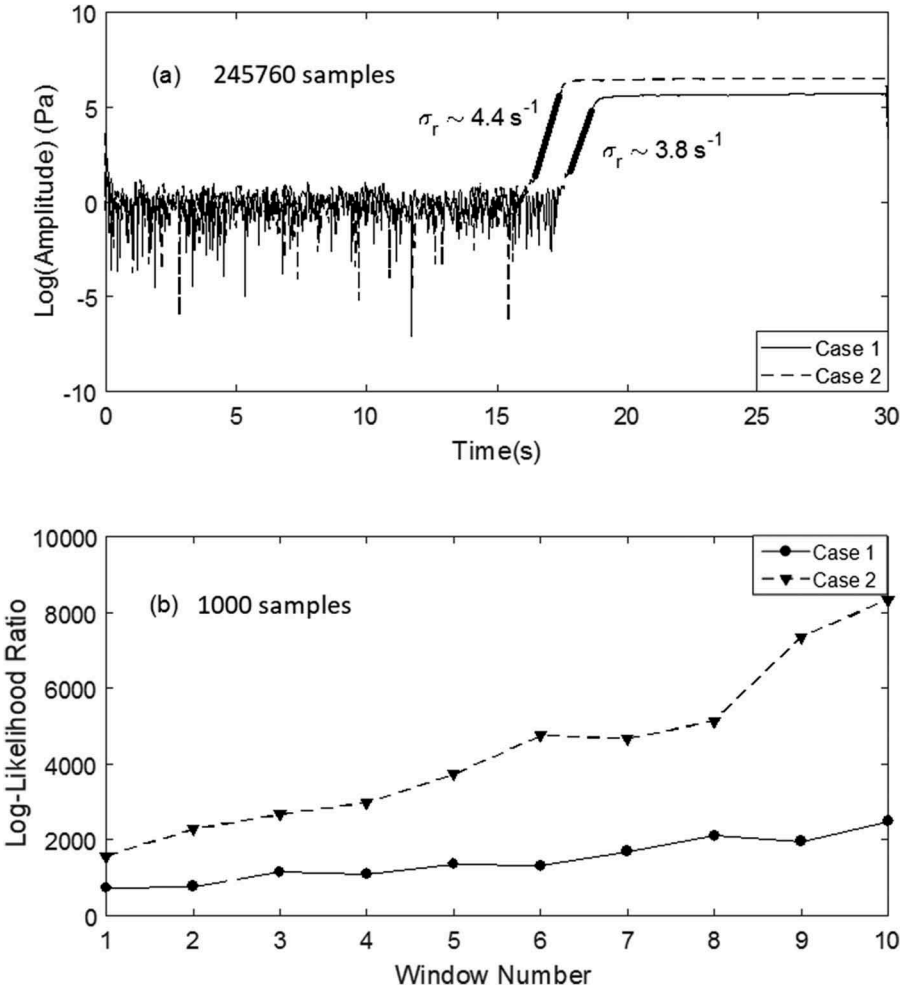

Figure 12. Comparison of growth rates with log-likelihood evolution. (a) Growth rate calculation using Hilbert envelope. (b) Variation of LLR $[L_2 - L_1]$ (see Eq. (19)) in an early growth period of the two cases.

ratio to measure the degree of complexity in the dynamic nature of the acoustic fluctuations with the onset of instability. Sarkar et al. (2016) proposed a data-driven technique of monitoring the state complexity of D-Markov machines which starts dropping as the combustion system tends to become unstable. This is consistent with the observations (Gotoda et al., 2012) with regard to variations in the complexity of the pressure data. Sarkar et al. (2016) also proposed a method of detecting instabilities by appropriately thresholding on the variation of the $\times D$-Markov entropy rates from heterogeneous sensors, namely, pressure and chemiluminescence data.

These methods have been applied for predictions of instability with respect to steady state response at different operating conditions, and they are, in a way, different from the method proposed in this paper which attempts to detect the growth of instabilities as a result of bifurcation resulting in the triggering of transient growth to limit cycles. However, it is still worth comparing the computational complexity of all these methods because they can be posed as potential competitors in their

applications to predicting the degree of instability in the steady state response of the combustion system. For example, with respect to the Rijke tube apparatus described in this paper, the steady state response of the system after a set point of power input is reached can be recorded and studied with two HMMs corresponding to stable and unstable modes of operation. With this domain knowledge incorporated in the training phase, LLR-based methods can be used to calculate the relative likelihoods of the steady state acoustic signature as a function of power inputs to study the degree of instability in the acoustic behavior. Table 2 compares the average online processing times of the techniques mentioned above with the time complexity of the LLR $[L_2 - L_1]$ calculation. The comparison is carried out in the MATLAB-2014 environment on a computation platform of Dell Precision T3400 PC with Intel(R) Core(TM) 2 Quad CPU Q9550 @ 2.83GHz and 2.83 GHz. As discussed earlier, the calculation of the likelihood $p(\mathbf{Y}|\lambda)$ using *Forward Algorithm* has a complexity of $\sim|\mathcal{Q}|^2T$. This is reflected in the almost linear increment of the processing time with respect to the data length for calculating the likelihood ratio $[L_2 - L_1]$ (dashed line with circles). The likelihood ratio computation time fares better than that of the minimum permutation entropy method, although the time complexities for the computation of both the Hurst Exponent and $\times D$-Markov entropy rate are lesser. However, it is worth mentioning here that HMMs are a class of more complex non-deterministic models representing the probabilistic behavior of temporal data and it can be used directly to solve the problem of regime detection with relatively short-length data, for which direct applicability of other methods have not been reported. Moreover, the HMM framework, in principle, can be trained with other classes of instabilities like lean blowout or screech with data generated from simulations/experiments, and hence can be extended for detection of various undesirable regimes of operation, subject to sufficient training experience. Also, the focal area of this paper is to portray the applicability of the HMM-LLR method for data lengths less than 1000 samples (~120 ms, with sampling frequency, F_s = 8192 Hz). Such short data lengths have not been used previously in the other aforementioned techniques for instability detection in stationary data. Table 3 lists the processing times for the online calculation of LLR using the different window lengths as described in Figure 6. Hence, the competitive time complexity of the HMM LLR along with its performance robustness even at very short data lengths makes it a

Table 2. Time complexity of different methods for detection of combustion instabilities.

	Processing times of different data-driven methods (s)			
Data length (s)	Hurst exponent	xD-Markov entropy rate	Minimum pemutation entropy	Log-likelihood ratio
0.2	0.019	0.056	0.095	0.035
0.4	0.025	0.059	0.135	0.068
0.6	0.031	0.062	0.174	0.011
0.8	0.035	0.065	0.213	0.132
1.0	0.041	0.068	0.252	0.164

Table 3. Time complexity of LLR calculation in the online phase.

Number of samples (F_s = 8192 Hz)	50	100	500	1000
Data length (ms)	6	12	60	120
Processing time (ms)	4	6	12	23

potentially suitable method for regime detection and instability classification, which is a key element for real-time detection and active control of combustion instabilities.

Summary, conclusions, and future work

This paper has developed and validated a non-deterministic statistical modeling tool for early detection of thermoacoustic instabilities and identification of operational regimes in combustion systems. The analysis is based on learning HMM to represent the typical behavior of the combustion system with data from different regimes, and using the models for predicting the most likely regime from a short test sequence of acoustic pressure recordings. This method focuses on real-time applications with short windows of pressure time series without compromising the accuracy of prediction of thermoacoustic instabilities and identification of the associated operational regimes. The proposed HMM-based method has been validated on experimental data from an electrically heated Rijke tube apparatus for predicting the onset of thermoacoustic instabilities. The results of the proposed method have been compared with those of similar data-driven techniques on the same data sets for estimating growth rates of thermoacoustically unstable systems (e.g., linear fitting from Hilbert envelope of the pressure time series). The proposed HMM-based method yielded consistent observations on the growth rate detection, albeit requiring significantly lower data history for its efficient implementation and applicability. While the proposed method is found to be robust with respect to spurious process and measurement noise, the response of the detection algorithm is sensitive to small changes in the regime characteristics, which makes it very suitable for detection of texture changes in the temporal signature of the acoustic data.

The proposed method is suitable for real-time anomaly detection and regime identification based on short-length time series of pressure oscillations. Since real-time active control of thermoacoustic instabilities (TAI) is a problem of major concern in the development of reliable combustion systems, the technique presented in this paper can serve as a computationally efficient tool for real-time detection of operational regimes from online measurements with parsimonious data requirements, making it a potentially effective for real-time active control of TAI.

While there are many areas of theoretical and experimental research to enhance the work reported in this paper, the authors suggest the following topics for future research:

(a) Development of a unified detection framework addressing other modes of instabilities (e.g., lean blowouts).
(b) Extension of the proposed HMM-based method for detection of instabilities in combustion systems operating under different kinds of protocols.
(c) Extension of the probabilistic approach in the reported work to state estimation for forecasting of future states for prediction of the temporal behavior.
(d) Implementation of the HMM-based method for (closed-loop) active control of the laboratory-scale apparatus with actuators for controlling instabilities.
(e) Enhancement of computational efficiency of the HMM-based method further by using variational inference-based learning of the probabilistic models (Murphy, 2012).

Pertinent acronyms

AUC	Area under the curve
DFT	Discrete Fourier transform
HMM	Hidden Markov modeling
LLR	Log-likelihood ratio
LPM	Liters per minute
ROC	Receiver operating characteristic
SNR	Signal to noise ratio
SDE	Stochastic differential equation
TAI	Thermoacoustic instabilities

Disclaimer

Any opinions, findings and conclusions or recommendations expressed in this publication are those of the authors and do not necessarily reflect the views of the sponsoring agencies.

Funding

The work reported in this paper has been supported in part by the U.S. Air Force Office of Scientific Research (AFOSR) under Grant Nos. FA9550-15-1-0400 and FA9550-18-1-0135 in the area of dynamic data-driven application systems (DDDAS).

References

Akaike, H. 1974. A new look at the statistical model identification. *IEEE Trans. Autom. Control*, **19** (6), 716–723. doi:10.1109/TAC.1974.1100705.

Bishop, C. 2007. *Pattern Recognition and Machine Learning*, Springer, New York, NY.

Boujo, E., Denisov, A., Schuermans, B., and Noiray, N. 2016. Quantifying acoustic damping using flame chemiluminescence. *J. Fluid Mech.*, **808**, 245–257. doi:10.1017/jfm.2016.663.

Celeux, G., and Durand, J.-B. 2008. Selecting hidden Markov model state number with cross-validated likelihood. *Comput. Stat.*, **23**(4), 541–564. doi:10.1007/s00180-007-0097-1.

Chen, J., Hsu, T.-Y., Chen, C.-C., and Cheng, Y.-C. 2011. Online predictive monitoring using dynamic imaging of furnaces with the combinational method of multiway principal component analysis and hidden Markov model. *Ind. Eng. Chem. Res.*, **50**(5), 2946–2958. doi:10.1021/ie100671j.

Fawcett, T. 2006. An introduction to ROC analysis. *Pattern Recognit. Lett.*, **27**(8), 861–874. ROC Analysis in Pattern Recognition. doi:10.1016/j.patrec.2005.10.010.

Gelbert, G., Moeck, J.P., Paschereit, C.O., and King, R. 2012. Feedback control of unstable thermo-acoustic modes in an annular rijke tube. *Control Eng. Pract.*, **20**(8), 770–782. doi:10.1016/j.conengprac.2012.03.016.

Gopalakrishnan, E.A., and Sujith, R.I. 2014. Influence of system parameters on the hysteresis characteristics of a horizontal rijke tube. *Int. J. Spray Combust. Dyn.*, **6**(3), 293–316. doi:10.1260/1756-8277.6.3.293.

Gotoda, H., Amano, M., Miyano, T., Ikawa, T., Maki, K., and Tachibana, S. 2012. Characterization of complexities in combustion instability in a lean premixed gas-turbine model combustor. *Chaos: Interdiscip. J. Nonlinear Sci.*, **22**(4), 043128. doi:10.1063/1.4766589.

Hajek, B. 2015. *Random Processes for Engineers*, Cambridge University Press, Cambridge, UK.

Hummel, T., Berger, F., Stadlmair, N., Schuermans, B., and Sattelmayer, T. 2017. Extraction of linear growth and damping rates of high-frequency thermoacoustic oscillations from time domain data. *ASME Turbo Expo: Power for Land, Sea, and Air*, Vol. 4A, Combustion, Fuels and Emissions. doi:10.1115/GT2017-64233. ISBN: 978-0-7918-5084-8

Jamieson, N.P., Rigas, G., and Juniper, M.P. 2017. Experimental sensitivity analysis via a secondary heat source in an oscillating thermoacoustic system. *Int. J. Spray Combust. Dyn.*, **9**(4), 230–240. doi:10.1177/1756827717696325.

Laera, D., Campa, G., Camporeale, S.M., Bertolotto, E., Rizzo, S., Bonzani, F., Ferrante, A., and Saponaro, A. 2014. Modelling of thermoacoustic combustion instabilities phenomena: application to an experimental test rig. *Energy Procedia*, **45**, 1392–1401. ATI 2013-68th Conference of the Italian Thermal Machines Engineering Association. doi:10.1016/j.egypro.2014.01.146.

Li, X., Zhao, D., Yang, X., Wen, H., Jin, X., Li, S., Zhao, H., Xie, C., and Liu, H. 2016. Transient growth of acoustical energy associated with mitigating thermoacoustic oscillations. *Appl. Energy*, **169**, 481–490. doi:10.1016/j.apenergy.2016.01.060.

Lieuwen, T. 2005. Online combustor stability margin assessment using dynamic pressure data. *J. Eng. Gas Turbines Power*, **127**(3), 478–482. doi:10.1115/1.1850493.

Lieuwen, T.C. 2003. Statistical characteristics of pressure oscillations in a premixed combustor. *J. Sound Vib.*, **260**(1), 3–17. doi:10.1016/S0022-460X(02)00895-7.

Lieuwen, T.C., and Yang, V. 2005. Combustion instabilities in gas turbine engines: operational experience, fundamental mechanisms, and modeling. *Am. Inst. Aeronautics Astronautics*, **1**, 3–26. chapter

Matveev, K. (2003), Thermoacoustic instabilities in the Rijke tube: experiments and modeling, PhD thesis, California Institute of Technology.

Menon, S., Uluyol, O., Kim, K., and Nwadiogbu, E.O. (2003), Incipient fault detection and diagnosis in turbine engines using hidden Markov models.

Moeck, J., Bothien, M., Paschereit, C., Gelbert, G., and King, R. (2007), Aerospace Sciences Meetings, American Institute of Aeronautics and Astronautics, chapter Two-Parameter Extremum Seeking for Control of Thermoacoustic Instabilities and Characterization of Linear Growth.

Mondal, S., Bhattacharya, C., Chattopadhyay, P., Mukhopadhyay, A., and Ray, A. (2017), AIAA propulsion and energy forum, American Institute of Aeronautics and Astronautics, Chapter: Prediction of Thermoacoustic Instabilities in a Premixed Combustor based on FFT-based Dynamic Characterization.

Mukherjee, K., and Ray, A. 2014. State splitting and merging in probabilistic finite state automata for signal representation and analysis. *Signal Process.*, **104**, 105–119. doi:10.1016/j.sigpro.2014.03.045.

Murphy, K. 2012. *Machine Learning: A Probabilistic Perspective*, 1st ed.. Cambridge, MA, USA: The MIT Press

Nair, V., and Sujith, R.I. 2014. Multifractality in combustion noise: predicting an impending combustion instability. *J. Fluid Mech.*, **747**, 635–655. doi:10.1017/jfm.2014.171.

Noiray, N., and Denisov, A. 2017. A method to identify thermoacoustic growth rates in combustion chambers from dynamic pressure time series. *Proc. Combust. Inst.*, **36**(3), 3843–3850. doi:10.1016/j.proci.2016.06.092.

Noiray, N., and Schuermans, B. 2012. Theoretical and experimental investigations on damper performance for suppression of thermoacoustic oscillations. *J. Sound Vib.*, **331**(12), 2753–2763. doi:10.1016/j.jsv.2012.02.005.

Noiray, N., and Schuermans, B. 2013. Deterministic quantities characterizing noise driven Hopf bifurcations in gas turbine combustors. *Int. J. Non Linear Mech.*, **50**, 152–163. doi:10.1016/j.ijnonlinmec.2012.11.008.

Poor, H.V. 2013. *An Introduction to Signal Detection and Estimation*. New York, NY, USA: Springer Science & Business Media.

Rabiner, L., and Juang, B.-H. 1993. *Fundamentals of Speech Recognition*, Prentice-Hall, Inc., Upper Saddle River, NJ.

Rabiner, L.R. 1989. A tutorial on hidden Markov models and selected applications in speech recognition. *Proc. IEEE*, **77**(2), 257–286. doi:10.1109/5.18626.

Rajagopalan, V., and Ray, A. 2006. Symbolic time series analysis via wavelet-based partitioning. *Signal Process.*, **86**(11), 3309–3320. doi:10.1016/j.sigpro.2006.01.014.

Ray, A. 2004. Symbolic dynamic analysis of complex systems for anomaly detection. *Signal Process.*, **84**(7), 1115–1130. doi:10.1016/j.sigpro.2004.03.011.

Rigas, G., Jamieson, N.P., Li, L.K.B., and Juniper, M.P. 2016. Experimental sensitivity analysis and control of thermoacoustic systems. *J. Fluid Mech.*, 787. doi.org/10.1017/jfm.2015.715

Rydén, T. 1995. Estimating the order of hidden Markov models. *Statistics*, **26**(4), 345–354. doi:10.1080/02331889508802501.

Sarkar, S., Chakravarthy, S.R., Ramanan, V., and Ray, A. 2016. Dynamic data-driven prediction of instability in a swirl-stabilized combustor. *Int. J. Spray Combust. Dyn.*, **8**(4), 235–253. doi:10.1177/1756827716642091.

Schwarz, G. 1978. Estimating the dimension of a model. *Ann. Statist.*, **6**(2), 461–464. doi:10.1214/aos/1176344136.

Stadlmair, N.V., Hummel, T., and Sattelmayer, T. (2017), Thermoacoustic damping rate determination from combustion noise using bayesian statistics, *ASME Turbo Expo 2017: Turbomachinery Technical Conference and Exposition* (50848), V04AT04A025.

Thompson, J., and Stewart, H. 1986. *Nonlinear Dynamics and Chaos*, John Wiley, Chichester, UK

Yi, T., and Gutmark, E.J. 2008. Online prediction of the onset of combustion instability based on the computation of damping ratios. *J. Sound Vib.*, **310**(1), 442–447. doi:10.1016/j.jsv.2007.07.072.

Combustion Theory and Modelling, 2020
https://doi.org/10.1080/13647830.2020.1714080

Reduced-order modelling of thermoacoustic instabilities in a two-heater Rijke tube

Chandrachur Bhattacharya[a], Sudeepta Mondal[a,b], Asok Ray[a,b*] and Achintya Mukhopadhyay[c]

[a]*Department of Mechanical Engineering, The Pennsylvania State University, University Park, PA, USA;* [b]*Department of Mathematics, The Pennsylvania State University, University Park, PA, USA;* [c]*Department of Mechanical Engineering, Jadavpur University, Kolkata, India*

(*Received 12 September 2019; accepted 18 December 2019*)

The topic of thermoacoustic instabilities in combustors is well-investigated, as it is important in the field of combustion, primarily in gas-turbine engines. In recent years, much attention has been focused on monitoring, diagnosis, prognosis, and control of high-amplitude pressure oscillations in confined combustion chambers. The Rijke tube is one of the most simple, yet very commonly used, laboratory apparatuses for emulation of thermoacoustic instabilities, which is also capable of capturing the physics of the thermally driven acoustics. A Rijke tube apparatus can be constructed with an electrical heater acting as the heat source, thus making it more flexible to operate and safer to handle than a fuel-burning Rijke tube or a fuel-fired combustor. Augmentation of the heat source of the Rijke tube with a secondary heater at a downstream location facilitates better control of thermoacoustic instabilities. Along this line, much work has been reported on the investigation of thermoacoustics by using computational fluid dynamics (CFD) modelling as well as reduced-order modelling for both single-heater and two-heater Rijke tube systems. However, since reduced-order models are often designed and built upon certain empirical relations, they may not account for the dynamic behaviour of the heater itself, which is a critical factor in the analysis and synthesis of real-time robust control systems. This issue is addressed in the current paper, where modifications have been made to existing models by incorporating heater dynamics. The model results are systematically validated with experimental data, generated from an in-house (electrically heated) Rijke tube apparatus.

Keywords: thermoacoustic instability; Rijke tube apparatus; reduced-order modelling

1. Introduction

The prime source of thermoacoustic instabilities (TAI) [1] in a combustor is the strong coupling between the unsteady heat release rate from fuel-air burning and natural acoustics in the confined combustion chamber. The TAI phenomena lead to high-amplitude pressure oscillations (e.g. peak values reaching $\sim$ 1000 Pa) in the combustion chamber, which could be detrimental to the structural integrity of the combustor as these oscillations may produce thermomechanical fatigue stresses in the combustor wall and liners. The TAI phenomena also cause disruptions in the air flow through the combustor, often leading to flow reversal (which affects both upstream and downstream components in the combustion

*Corresponding author. Email: axr2@psu.edu

system as well) and instigating flame blowout. It is well known that a very small amount of energy from the combustion process may lead to TAI due to low acoustic damping in the combustors [2].

In recent years, much research has been conducted to investigate the nonlinear nature of acoustic waves within the combustion chamber. The Rijke tube [3] is one of the simplest experimental devices that can capture the essential physics of combustion chamber acoustics and their coupling with the heat release rate. A thorough experimental and numerical study on Rijke tubes has been conducted by [4]. Other researchers such as [5–7] have also conducted studies using a Rijke tube apparatus and have attempted to implement various control methods in order to reduce the severity of TAI. Several researches (e.g. [8–12]) have also conducted experimental research on TAI in fuel-burning laboratory-scale combustors. However, a major drawback of solely using an experimental apparatus for the purpose of extensive research is the lack of versatility and operating range, which is primarily due to safety requirements or limitations of the facilities at hand. Thus, there is a strong need for the development of reduced-order numerical models for the study of combustion instabilities in the framework of computational models of affordable complexity. [13] proposed a simplified reduced-order model based on the principle of Galerkin-type modal decomposition of the acoustic waves to solve the acoustic wave equation with a heat source. A similar method has been used by [14,15] for modelling the Rijke tube. Most current available Galerkin-based models try to account for the heater time lag using a variable τ (e.g. [16]). However this is a flow time lag and does not include the time response of the heater itself, i.e. the thermal inertia of the system or the dynamics of the heater; moreover, estimating of the parameter τ is not always easy. This may lead to moderately inaccurate response times, which is an important factor in designing a robust online active control system. In the research work reported in the current paper, the authors have attempted to modify the existing Galerkin-based numerical model to include heater and thermal dynamics as well as include some of the flow physics to provide more accurate time responses, while still retaining much lower model complexity than a full-scale computational fluid dynamics (CFD) simulation. In the models available in the literature, the user needs to specify parameters such as heater temperature, which cannot be directly controlled. The model, proposed in this paper, uses heater power as an input to the system, similar to the input that an experimental Rijke tube apparatus receives. Similarly, the reduced-order model is re-formulated such that, for the same model parameters, the entire range of operation of the Rijke tube can be simulated without re-tuning the critical parameters.

Several methods exist for suppression of the generated high-amplitude pressure oscillations in combustors. Passive control in the form of acoustic dampers [17] are widely used for mitigation of TAI. However, such acoustic dampers are only useful over certain frequency ranges, and they may not be effective at low frequencies. Several active control methods have also been proposed by researchers, such as the use of Helmholtz resonators [18], loudspeakers [7,14] and radial injection of air through micro-jets [19]. Usage of a secondary heat source has been introduced by [20] as a method of controlling the TAI based on the concept of destructive interference. This is a viable method of TAI control, especially for large combustors in aircraft and land-based gas turbines. Numerical simulations have been conducted in the current paper to investigate the efficacy of using a secondary (control) heater downstream for mitigating the instabilities of pressure oscillations in the Rijke tube.

Contributions: From the above perspectives, major contributions of the paper are summarised below.

(1) *Modification of established modal decomposition-based order reduction techniques*: The objective here is to include the effects of heater dynamics, system thermal inertia, and flow dynamics on the reduced-order model.
(2) *Modification of the simulation procedure for reduced-order modelling*: The objective here is to develop a numerically efficient procedure that takes into account the effects of time-varying thermal and flow conditions of the Rijke tube apparatus for numerical solution.
(3) *Demonstration of the efficacy of a secondary control heater as a method for suppressing the instabilities in the Rijke tube system*: The objective here is to show how the results of the numerical simulation compare to those reported in the standard literature.
(4) *Experimental validation of the proposed reduced-order modelling technique*: The objective here is to validate the aforesaid model against experimental results from an in-house Rijke tube and to show how the designed formulation works across the entire operational regime.

Organisation: The rest of the paper is organised into the following sections:

- Section 2 describes the Rijke tube apparatus that is used to produce the experimental data for validating the proposed numerical model.
- Section 3 presents the basic mathematical formulation of a reduced-order Galerkin-based model of the two-heater Rijke tube, where the modifications pertaining to the thermal inertia effects are also described. Section 3.4 validates the proposed numerical model with the results that are obtained from the experiments.
- Section 4 discusses the stability chart that is generated from the experimental data. Section 4.4 briefly discusses the hysteresis effects as seen in the numerical model, and also provides a comparison with the results of experimental studies that are reported in the literature.
- Section 5 demonstrates selected numerical simulations by using the secondary heater as a control mechanism for suppression of instabilities, where the results are compared to those available in the reported literature.
- Section 6 summarises and concludes the paper along with recommendations for future research.

2. The experimental Rijke tube apparatus

The experimental Rijke tube apparatus, which has been constructed in the laboratories of Penn State [21], consists of a 1.5 m long aluminium tube with a hollow square cross-section of inside lengths of 93 mm. There are two heating elements: a fixed primary heater at 0.375 m from the flow inlet and a movable secondary heater downstream. Both heaters are made of compact wire-mesh Nichrome for generating thermal power, which emulate the flame in a combustible fuel-air mixture in a real-life combustor. The secondary (control) heater has a maximum displacement of 500 mm from the centre of the tube towards the exit end. Figure 1 depicts the Rijke tube apparatus.

An array of eight wall-mounted pressure sensors are placed at equidistant axial locations for capturing the pressure signals. The Rijke tube data are acquired at a sampling rate

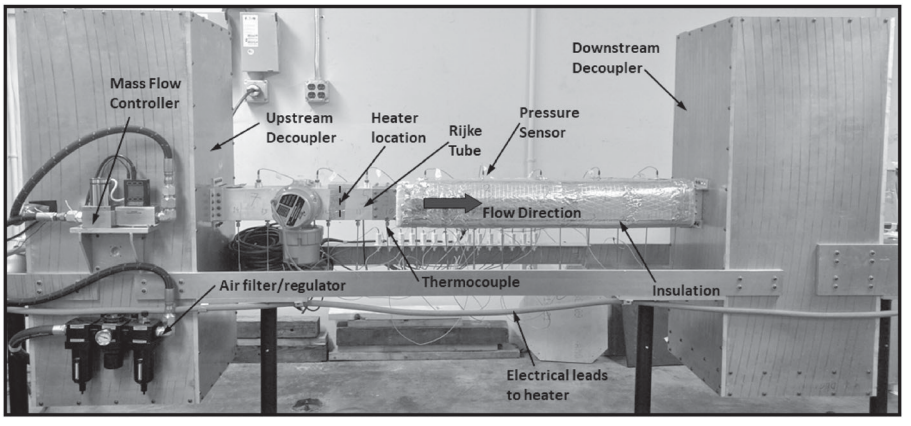

Figure 1. Rijke tube experimental apparatus.

of 8192 Hz. To measure the spatio-temporal temperature variation, 15 K- type transition-junction thermocouple probes are used. The mass-flow rate into the system is controlled accurately using an Alicat Mass Flow Controller (0–1000 SLPM). The mass-flow rate controls not just the velocity over the heater but also affects the convective heat transfer from the wire mesh to the air and heat loss to the walls. The inlet and outlet of the tube are fitted with decouplers, which are large hollow enclosures serving the purpose of producing pressure waves under open-open end boundary conditions of the Rijke tube. Additionally, the upstream decoupler reduces flow fluctuations at the inlet while the downstream decoupler serves as a heat sink, allowing the hot air exiting the outlet to be cooled, before it is released to the atmosphere.

The two Nichrome heaters are capable of handling high heating loads for a sufficiently long time without being oxidised at the high operating temperatures. The square-weave 40-mesh structure of each heater acts as an acoustically compact source of thermal energy and allows a uniform heating of air over a cross-section. Two copper rods are welded to the copper strips and are electrically shielded from the walls of the chamber. The copper tubes are connected to a programmable DC power supply. The length of the tube downstream of the heater is insulated to prevent heat loss from the walls allowing for maintaining the same initial and running conditions of different experimental runs. It also acts as a safety measure to prevent the operator from coming in contact with the hot metal walls.

3. Reduced-order numerical modelling of the Rijke tube

This section addresses reduced-order modelling of both single-heater and two-heater Rijke tubes, which include the thermal-hydraulic dynamics and their coupling with chamber acoustics.

3.1. *Modelling of a single-heater Rijke tube*

As mentioned previously, a simplified reduced-order model using Galerkin-type modal decomposition was introduced by [13,22] to solve the acoustic wave equation with a heat source in the system. The one-dimensional wave equation was derived for the pressure

perturbations (p') as

$$\frac{\partial^2 p'}{\partial t^2} - a^2 \frac{\partial^2 p'}{\partial x^2} = (\gamma - 1)\frac{\partial \dot{Q}}{\partial t} \tag{1}$$

where a denotes the speed of sound and $\dot{Q}$ is the volumetric rate of thermal power addition. Equation (1) does not include the effects of mean flow on the acoustic field. Culick's expansion [13] is used for the pressure perturbations (p') and velocity perturbations (u') using the Galerkin eigen-acoustic modes. The decomposition into n modes having individual time-varying modal amplitudes of $\eta_j(t)$ yields:

$$p'(x,t) = \sum_{j=1}^{n} p'_j(x,t) = p_0 \sum_{j=1}^{n} \eta_j(t)\psi_j(x) \tag{2}$$

$$u'(x,t) = \sum_{j=1}^{n} u'_j(x,t) = \sum_{j=1}^{n} \frac{\dot{\eta}_j(t)}{\gamma k_j^2}\frac{\mathrm{d}\psi_j(x)}{\mathrm{d}x} \tag{3}$$

where p_0 is the mean undisturbed pressure; $\psi_j(x)$ and k_j are the mode shape (at the location x) and the wavenumber of the jth mode, respectively, which has a natural frequency of ω_j; and γ is the ratio of specific heats of air.

Substituting Equation (2) into Equation (1), expanding into eigen-modes, and adding a damping term ξ_j [23], the final expression is obtained as

$$\frac{\mathrm{d}^2\eta_j}{\mathrm{d}t^2} + 2\xi_j\omega_j\frac{\mathrm{d}\eta_j}{\mathrm{d}t} + \omega_j^2\eta_j = \frac{\gamma - 1}{p_0}\int \psi_j \frac{\partial \dot{Q}}{\partial t}\mathrm{d}x \tag{4}$$

where the left-hand expression in Equation (4) represents a set of n uncoupled linear oscillators that are excited by the forcing terms on the right-hand side. For a Rijke tube, [14] proposed a modified version of King's law, which yields the volumetric rate of heat addition ($\dot{Q}$) as

$$\dot{Q} = \frac{2L_w(T_w - \overline{T})}{SL\sqrt{3}}\sqrt{\pi\lambda C_v\rho_0\frac{d_w}{2}}\left[\sqrt{\left|\frac{u_0}{3} + u'_f(t-\tau)\right|} - \sqrt{\left|\frac{u_0}{3}\right|}\right]\delta(x - x_f) \tag{5}$$

where L is the length of the Rijke tube, L_w is the equivalent length of the wire, λ is the thermal conductivity of air, C_v is the constant volume specific heat capacity of air, τ is the time lag between the heat transfer and the velocity as a result of thermal inertia, ρ_0 is the mean density of the Rijke tube air, d_w is the heater wire diameter, $(T_w - \overline{T})$ is the mean temperature difference between the heater and the air, S is the cross-sectional area of the Rijke tube, x_f is the heater location, and u'_f is the acoustic velocity perturbation at the heater location. Using Equation (5), the acoustic equation (Equation (4)) is modified to:

$$\frac{\mathrm{d}^2\eta_j}{\mathrm{d}t^2} + 2\xi_j\omega_j\frac{\mathrm{d}\eta_j}{\mathrm{d}t} + \omega_j^2\eta_j = \frac{\mathrm{d}\dot{Q}'}{\mathrm{d}t} \tag{6}$$

where $\dot{Q}'$ combines the remaining terms as

$$\dot{Q}' \triangleq \frac{2(\gamma - 1)L_w(T_w - \overline{T})}{p_0 SL\sqrt{3}}\sqrt{\pi\lambda C_v\rho_0\frac{d_w}{2}}\left[\sqrt{\left|\frac{u_0}{3} + u'_f(t-\tau)\right|} - \sqrt{\left|\frac{u_0}{3}\right|}\right]\psi_j(x_f) \tag{7}$$

and the frequency-dependent damping ξ_j is given by [4] as

$$\xi_j \triangleq \left(c_1 \frac{\omega_j}{\omega_1} + c_2 \sqrt{\frac{\omega_1}{\omega_j}} \right) \tag{8}$$

where the first term in Equation (8) is responsible for the end losses and the second term represents losses due to boundary layers; and the constants c_1 and c_2 are the damping coefficients that represent the amount of acoustic damping in the Rijke tube. The time lag τ is computed by using Lighthill's correlation as: $\tau \simeq 0.2 \frac{d_w}{u_0}$.

The modal equations, derived above, can be cast in a linearised state-space form and the dimensionality of the ordinary differential equation (ODE) system depends on the number of the selected 'significant' acoustic modes. For each mode, there are two states, η_j and $\dot{\eta}_j$. This ODE system can be solved using a numerical method (e.g. Runge-Kutta).

3.2. *Modelling of a two-heater Rijke tube*

A secondary heat source is introduced in the Rijke tube in addition to the primary heat source, with the secondary heater acting as a control heater. This arrangement changes Equation (6) to now having two heat source terms:

$$\frac{\mathrm{d}^2 \eta_j}{\mathrm{d}t^2} + 2\xi_j \omega_j \frac{\mathrm{d}\eta_j}{\mathrm{d}t} + \omega_j^2 \eta_j = \frac{\mathrm{d}\dot{Q}'_1}{\mathrm{d}t} + \frac{\mathrm{d}\dot{Q}'_2}{\mathrm{d}t} \tag{9}$$

$$\dot{Q}'_i = \frac{2(\gamma - 1) L_w (T_{w,i} - \overline{T})}{p_0 S L \sqrt{3}} \sqrt{\pi \lambda C_v \rho_0 \frac{d_w}{2}} \times \left[\sqrt{\left| \frac{u_0}{3} + u'_{f,i}(t - \tau_i) \right|} - \sqrt{\left| \frac{u_0}{3} \right|} \right] \psi_j(x_{f,i}), \quad i = 1, 2 \tag{10}$$

where the subscript i takes values 1 and 2 for the primary and secondary heaters, respectively.

3.3. *Modelling of the heater and thermal dynamics*

The state-space representation of the acoustics in Equation (4) for the jth mode is

$$\begin{bmatrix} \dot{\eta}_j \\ \ddot{\eta}_j \end{bmatrix} = \begin{bmatrix} 0 & 1 \\ -\omega_j^2 & -2\xi_j \omega_j \end{bmatrix} \begin{bmatrix} \eta_j \\ \dot{\eta}_j \end{bmatrix} + \begin{bmatrix} 0 \\ \frac{d\dot{Q}'_1}{dt} + \frac{d\dot{Q}'_2}{dt} \end{bmatrix} \tag{11}$$

where the frequency ω_j, computed from [13,24], is represented as

$$\omega_j = a k_j \tag{12}$$

where the wavenumber k_j is fixed for a given acoustic boundary condition with input–output specifications of a (pressure anti-node, or pressure open) fixed inlet velocity and (pressure node, or pressure closed) constant outlet pressure; and the speed of sound a is

a function of the gas temperature in the tube. In this case, the tube has constant pressures at either end, and the speed of sound a is approximated to depend on the mean gas temperature, which yields the following expressions for ω_j and ξ_j:

$$\omega_j = \sqrt{\gamma R\, T_{avg}}\left(j\frac{\pi}{L}\right) \tag{13}$$

$$\frac{\xi_j}{\xi_1} = \frac{\omega_j}{\omega_1} \tag{14}$$

Since ω_j directly depends on the time-dependent temperature T, the system matrix in Equation (11) is linear parameter varying (LPV) (which is effectively time varying) and hence needs to be recomputed at each time step.

For ease of computation, many researchers have used the above reduced-order equations by making certain approximations, such as the mean values of temperature and flow velocity, under the assumption that they are constants. However, this assumption may not always be appropriate, not only because of the temporal changes but also due to the rate of change of these time-dependent parameters. In the experimental apparatus, it may not be possible to control directly the temperature of the heaters, but instead the power input into the heater is the directly controllable variable and the temperature changes occur as a result of the power input and the heat transfer within the Rijke tube. Therefore, the temperature itself has its own dynamics, which has been addressed in this paper and included into the computational procedure.

In view of the above discussion, the heater power is the variable that is set by the user, and the temperatures evolve following the various relations of heat transfer and fluid mechanics. In the experimental apparatus, the power supply has its own transient behaviour, which is assumed to be linear within the operational range such that the heater is able to go from 0 to 2000 W in a linear ramp in 1 s; and this limits the rate of power rise or fall in the heaters. The rate of heat loss ($\dot{Q}_{heater}$) from the heater in a time step is computed from the following equation [15]:

$$\dot{Q}_{heater}(t) = L_w(T_{w,i} - \overline{T})\left[\lambda + 2\sqrt{\pi\lambda C_v \rho_0 \frac{d_w}{2}}\left(\left(1 - \frac{1}{3\sqrt{3}}\right)\sqrt{\overline{u}} + \frac{1}{\sqrt{3}}\sqrt{\left|\frac{\overline{u}}{3} + u'(t-\tau)\right|}\right)\right] \tag{15}$$

So the temperature of the heater wire (T_w) changes in the time interval $[t,\ t + \mathrm{d}t)$ as

$$T_w \leftarrow T_w + \frac{(P(t) - \dot{Q}_{heater}(t))\,\mathrm{d}t}{MCp_{wire}(T_w)} \tag{16}$$

where M is the mass of the wire mesh that can be obtained by measurement; $P(t)$ is the time-dependant power supplied to the heater; and Cp_{wire} is the (temperature-dependent) specific heat capacity of the wire material, which is available from manufacturer's specifications. For computing the temperature in the Rijke tube, the flow domain in the tube is split into three segments; one containing the volume between the inlet and first heater, the next being the volume between the two heaters, and the third being the volume between the secondary heater and the outlet. It is assumed that the temperature in the first segment is always the same as the inlet temperature (T_{in}). The temperatures in the remaining

two sections are computed by doing energy flow analysis on the constant volume; $\dot{Q}_{add}$ is the power added to a segment in a time step, where the subscript *down* denotes the value downstream:

$$\dot{Q}_{add} = Cp(T_{down})T_{down}\dot{m}_{in} + \dot{Q}_{heater}(t) - \dot{Q}_{conv} - Cp(T_{segment})T_{segment}\dot{m}_{in} \tag{17}$$

where $\dot{Q}_{conv}$ is the rate of heat loss to the Rijke tube wall of area $A_{segment}$ (which is at the inlet temperature) via convection.

$$\dot{Q}_{conv} = 0.664\lambda(Re_{segment})^{0.5}(Nu)^{0.333}A_{segment}(T_{segment} - T_{in}) \tag{18}$$

Finally, the temperature of the volume segment $V_{segment}$ is computed in the time interval $[t,\ t + \mathrm{d}t)$ as

$$T_{segment} \leftarrow T_{segment} + \frac{\dot{Q}_{add}\,\mathrm{d}t}{\rho V_{segment} Cp(T_{segment})} \tag{19}$$

The average temperature is measured as the segment length-weighted average of the segment temperatures.

Using all the above additional information that is computed by solving the heat transfer and certain fluid equations, the reduced-order model can be improved by removing some of the typical assumptions. Values of parameters (e.g. the mean temperature, wire temperature, density and velocity at the wire) now become functions of time and are dependent on the changing operating conditions of the Rijke tube. This is in agreement with what is observed experimentally as for the same heater input, the heater wire temperature is substantially higher when the flow rate is low due to lower convective heat transfer as opposed to higher flow rate situations. These physical processes also dictate mean temperature, speed of sound and the natural frequency of the system. Thus, a single model can be used for the entire operational range of the Rijke tube without having to make assumptions and change the individual variable values for each operating region. Furthermore, accounting for heater lag produces a more accurate time response of the system to changes in the control power and thus is better for studying transient phenomena or for testing the effectiveness of controllers on the system.

Equations (10) and (15) are modified to account for the local conditions of temperature and density as follows. The assumption here is that only the upstream values are considered when computing the heat transfer, where the subscripts *in* and *down* denote the values at the inlet and the downstream sections, respectively. It is noted that the model parameters C_v and λ are functions of temperature.

$$\dot{Q}_{heater}(t) = L_w(T_{w,i} - T_{down}) \times \left[\lambda + 2\sqrt{\pi\lambda(T)C_v(T)\rho_{in}\frac{T_{in}}{T_{down}}\frac{d_w}{2}}\right.$$
$$\left.\times\left(\left(1 - \frac{1}{3\sqrt{3}}\right)\frac{u_{in}T_{down}}{T_{in}} + \frac{1}{\sqrt{3}}\sqrt{\left|\frac{u_{in}T_{down}}{3T_{in}} + u'(t-\tau)\right|}\right)\right] \tag{20}$$

$$\dot{Q'}_i = \frac{2(\gamma-1)L_w(T_{w,i} - T_{down})}{\sqrt{3}p_{in}SL}\sqrt{\pi\lambda(T)C_v(T)\rho_{in}\frac{T_{in}}{T_{down}}\frac{d_w}{2}}$$
$$\times\left[\sqrt{\left|\frac{u_{in}T_{down}}{3T_{in}} + u'_{f,i}(t-\tau_i)\right|} - \sqrt{\left|\frac{u_{in}T_{down}}{3T_{in}}\right|}\right]\psi_j(x_{f,i}) \tag{21}$$

The effects of uncertainties are realised in the simulation by modifying the acoustic velocity perturbation u' with a zero-mean additive Gaussian noise component that is chosen to have an intensity equal to 0.5% of the mean flow velocity.

3.4. *Parameterisation of the reduced-order model*

This section parameterises the reduced-order model, developed in Section 3, to match the Rijke tube apparatus described in Section 2. The geometry and other model parameters are chosen to be the same as those in the experimental apparatus. The length of the numerically modelled Rijke tube is taken to be $L = 1.5\,\text{m}$, area of cross-section $S = 0.093 \times 0.093\,\text{m}^2$. The primary heater is placed at $x_1 = 0.375\,\text{m}$, similar to the experimental apparatus, and the pressure sensor is located at $x_p = 1\,\text{m}$; all lengths are measured downstream from the inlet. The heaters have properties similar to the actual wire mesh used in the experiment with $L_w = 23.6\,\text{m}$, $d_w = 0.33\,\text{mm}$. The thermal heat capacity is taken to be that of Nichrome and each wire mesh has a total mass of $M = 170\,\text{gm}$. The thermal properties of air used are fourth-order polynomials obtained from a NASA report (the NASA polynomials) [25].

In the numerical simulations reported in this paper, a total of 10 eigen-modes are considered to adequately capture the dynamics of the acoustic system. This implies that the number of eigen-modes is $n = 10$, as seen in Equations (2) and (3). To model the damping coefficients in Equation (8), the parameters c_1 and c_2 that are to be set by the user depend on the actual observed damping. These parameters have been set to be $c_1 = 0.048$ and $c_2 = 0.040$ to match the experimental results described in Section 4. Furthermore, the entire amount of the net heat transferred from the heater(s) enters the air, because a part of it is lost to the surroundings (primarily by radiation). Therefore, a factor $\alpha < 1$ is multiplied to the value of $Q(t)$. An empirical model of the parameter α is

$$\alpha = 1 - \left(\frac{T_w - T_{avg}}{T_w} \right)^{0.15} \tag{22}$$

The above formulation assumes the system to be acoustically closed. However, that is not actually true as though the presence of the decouplers maintain nearly constant pressures at the ends, the presence of a flow rate regulator ensures a constant flow. Thus, the average flow deviates from that computed directly in terms of the measured flow rate in LPM. Instead the flow velocity is obtained by multiplying the computed value of U_{in} by a scaling factor β that is empirically defined as $\beta = |U_{in}/U_{in}^*|^{0.9}$, where $U_{in}^* \triangleq 1\,\text{m/s}$, making β a dimensionless quantity. A zero-mean Gaussian noise of standard deviation $0.3Pa$ has been added to the output in order to emulate the process noise as well as the sensor noise. This choice is made to match the (non-dimensional) P_{rms} value described in Section 4.3. The numerical sensor measures the acoustic pressure of each Galerkin-mode and then computes the combined acoustic pressure at that location following Equation (2).

For the remainder of the paper, the parameter values described in this section have been used without any changes. In other words, with these parameters optimised a complete model of the system is obtained, and the only changes that need to be made for each numerical experiment are the boundary conditions.

E_{in} (W) / Q (LPM)	61	72	82	92	102	112	122	132	142	152	162	172	182	191	200	210	219	228	237	246	255	264	273	281	290
2000	o	o	o	o	o	o	o	x	x	x	x	x	x	x	x	x	x	x	x	x	o	o	o	o	o
1800	o	o	o	o	o	o	o	x	x	x	x	x	x	x	x	x	x	x	x	o	o	o	o	o	o
1600	o	o	o	o	o	o	o	o	x	x	x	x	x	x	x	x	x	x	o	o	o	o	o	o	o
1400	o	o	o	o	o	o	o	o	x	x	x	x	x	x	x	x	o	o	o	o	o	o	o	o	o
1200	o	o	o	o	o	o	o	o	x	x	x	x	x	x	x	o	o	o	o	o	o	o	o	o	o
1000	o	o	o	o	o	o	o	o	x	x	x	x	x	x	o	o	o	o	o	o	o	o	o	o	o
800	o	o	o	o	o	o	o	o	o	o	o	o	o	o	o	o	o	o	o	o	o	o	o	o	o
600	o	o	o	o	o	o	o	o	o	o	o	o	o	o	o	o	o	o	o	o	o	o	o	o	o
400	o	o	o	o	o	o	o	o	o	o	o	o	o	o	o	o	o	o	o	o	o	o	o	o	o
200	o	o	o	o	o	o	o	o	o	o	o	o	o	o	o	o	o	o	o	o	o	o	o	o	o

Figure 2. Stability map generated from experimental data of Rijke tube apparatus. Instability indicated by dark shading marked with ' × ', and stability by light shading with '○'.

4. Stability maps developed from experimental data and model data

This section develops and compares stability maps from data generated from the Rijke tube apparatus (see Section 2) and reduced-order model (see Section 3.4) under the same operating conditions.

4.1. *Stability map: experimental data*

Experiments have been conducted with multiple combinations of heater power input (E_{in}) and air flow rate (Q) to record data of 30 s duration for each case. A typical stability map is shown in Figure 2 with the following notations: the spaces marked as ' × ' (with a darker shaded box) denote unstable operation with an audibly discernible resonating mode, and those marked as '○' (with lighter shading) denote stable operation.

Different values of initial temperatures affect the stability characteristics of the thermoacoustic process as a consequence of changes in the mean temperature in the Rijke tube. When a lower initial mean temperature of around $\sim 300^{\circ}$K is maintained in the Rijke tube apparatus, a lower frequency (~ 114 Hz) mode of instability is observed; the instability occurred at a higher frequency (~ 131 Hz) mode at a higher initial mean temperature of $\sim 348^{\circ}$K. These observations are attributed to the increase in the speed of sound at an elevated mean temperature, which changes the fundamental frequency from an analytically calculated value of 115– 127 Hz for an open-open tube, tallying closely with the peak frequencies of experimental data. In this work, only the higher initial temperature mode has been reported for validation because it is more consistent and is easier to obtain experimentally because cooling the Rijke tube after each experiment is very time-consuming.

4.2. *Stability map: numerical simulation of the reduced-order model*

The reduced-order model, described in Section 3, has been run with the same model parameters for the same range of flow rates and primary heater power inputs as the experiments described above. The ambient temperature is taken to be 348°K, which is the more appreciable ambient conditions as described above. Each simulation has been performed for simulated time intervals of 30 s with a time step size $\Delta t = 10^{-4}$ s; and the root mean square (RMS) values of pressure oscillations are computed over the last 2 s as a measure of stability. An operational condition is considered to be unstable if the P_{rms} exceeds a threshold

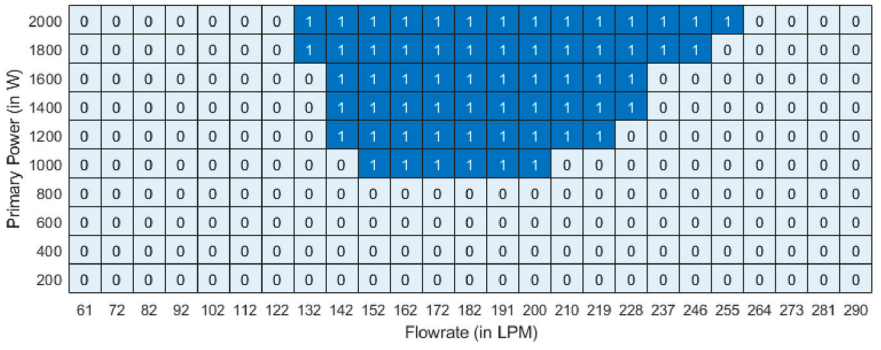

Figure 3. Stability map generated from simulation data of reduced-order model. Instability indicated by dark shading marked with '1', and stability by light shading with '0'.

of 5 Pa. The generated stability map is shown in Figure 3. The boxes shaded darker blue with the Boolean value of 1 indicates an unstable operating condition.

It is seen that the stability map matches very closely with that reported from experiments (shown in Figure 2). A comparison of the stability in Figures 2 and 3 reveals that, in the physical experiments, the maximum range of unstable operation is bounded in the power range 1000– 2000 W and in flow range 132–246 LMP. For the numerical simulation, the power range 1000–2000 W is identical to that in experiments, while the flow rate range is 132–255 LPM, which is reasonably close. The frequency of the unstable mode was also found to be 117 Hz which is very close to the experimentally obtained value of 131 Hz.

A comparison of the experimental stability map and numerical stability map reveals that the discrepancies occur for 7 out of 57 unstable conditions, yielding an error rate of about 12%. This discrepancy is possibly due to the fact that the numerical model is a deterministic model of a stochastic process with a few outliers. In addition, there may be certain experimental uncertainties such as the exact ambient temperature, the exact initial condition of the tube, both of which are not perfectly repeatable. There are also some modelling simplifications that may tend to lead to inaccuracies towards the edges of the unstable region seen in the stability map. However, for the purpose at hand, a higher-fidelity model may not be necessary because this low-fidelity model yields a sufficiently close match to the experimental ground truth. For another Rijke tube, the parameters (e.g. damping coefficients c_1 and c_2) of the numerical model should be tuned to match the experimental data.

It is also worthwhile to note that although theproposed reduced-order model is more detailed than the traditional Galerkin-based models (which do not account for heater effects or thermal inertia), the time required to run a simulation is reasonably low. In practice, it is observed that the simulation time required is approximately 1.5× (i.e. simulation of a time interval of 30 s takes ∼ 45 s of the machine run-time). The code has been developed and run on MATLAB 2019b utilising a single core of an Intel Xeon Workstation using the E5-2670 chipset.

4.3. *Comparison of numerical simulation and experimental results*

A major focus of this paper is to incorporate the thermal inertia of the heaters in the model equations and to investigate the effects of the same on the system dynamics of the Rijke tube. In order to study these phenomena, each experiment has been conducted

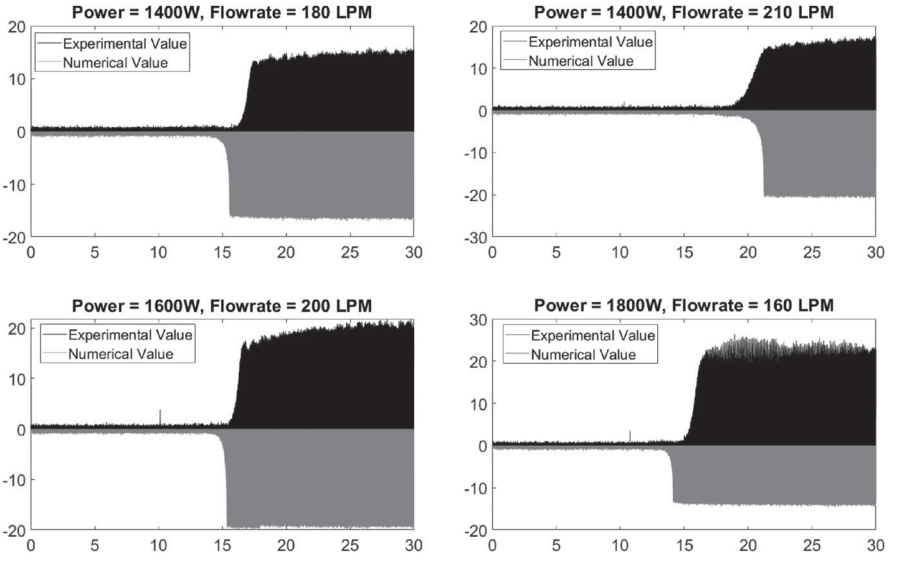

Figure 4. Time series of pressure oscillations: experimental and simulation data, where the upper parts (in black) are experimentally observed time series and the lower parts (in grey) are numerically simulated from the reduced-order model under the same operating conditions.

for a duration of 30 s in the following fashion. The heater power is maintained at 200 W for the first 10 s and then the heater power is abruptly increased to the final value. It is noted that the resulting increase in the heater temperature is not linear over the entire period. Furthermore, there is a process-dependent time delay between the heater power and heater temperature responses. As mentioned before, many reduced-order numerical models do not capture this behaviour. The model proposed in this paper incorporates the heater dynamics, and thus captures these delays in the formulation of the reduced-order model.

The four plates in Figure 4 display four profiles of pressure oscillations to compare the dynamic behaviour of the Rijke tube both in the experiment as well as in the numerical simulation under four different operating conditions. The primary power is maintained at 1400, 1600 and 1800 W as shown in the figure. For all of these runs, the secondary heater is kept inactive. For each of the operating condition reported here, the upper part (in black) of Figure 4 shows the pressure profile obtained from experiments following the same power profile. The lower part (in grey) of Figure 4 shows the equivalent numerical simulation. These responses have been scaled for ease of comparison, where the scaling factor has been chosen to be the root mean square (RMS) value of the noise. With this scale factor, the peak values of the numerically obtained instabilities match those that are obtained experimentally; from these observations, the noise in the reduced-order model is identified to be a zero-mean Gaussian with intensity 0.3 Pa.

Form the results of comparisons in Figure 4, it is concluded that the model-predicted instability growth is very close to that observed in the experimental results. This observation suggests that the numerical model is capable of capturing the Rijke tube dynamics very well, which include heater dynamics and delays. The small deviations between the model predictions and experimental observations, as seen in Figures 2 and 3 and in the four plates of Figure 4, can be attributed to the uncertainties in modelling of experimental conditions.

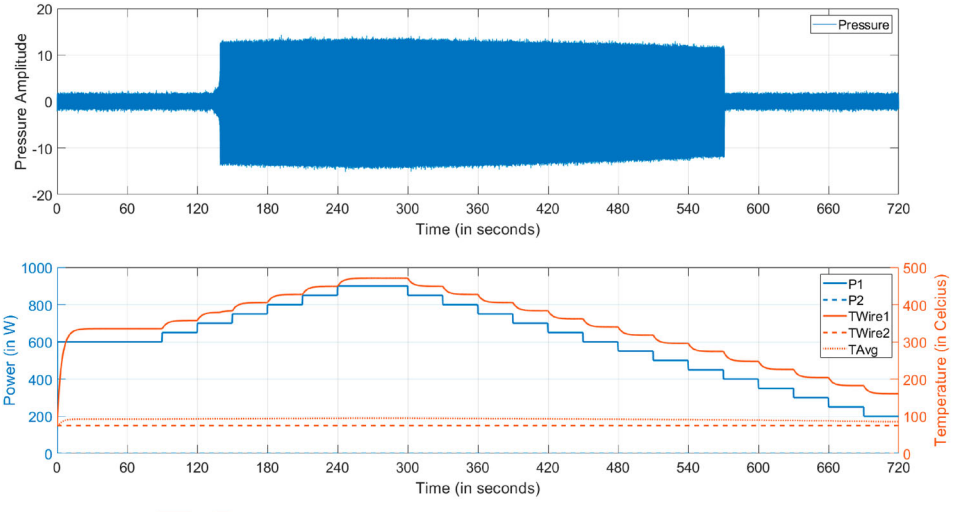

Figure 5. Time series of hysteresis experiment simulation.

4.4. *Hysteresis as a result of thermal dynamics*

It has been observed by [4] that the onset of instability in the Rijke tube exhibits hysteresis due to the thermal inertia of the system. The rationale is that the direction of approaching a particular operating condition may change depending on whether that it is stable or unstable; this effect is seen in the simulation as well. In order to observe the hysteresis phenomena, the simulation has been conducted for a total of 720 s duration when the air flow rate is held constant at 160 LPM and the primary heater power is varied in the following way. For the first 90 s, the primary heater power is held at 600 W to ensure that a steady state is reached. Subsequently, the primary heater power is increased in steps of 50 W on an interval of 30 s. Holding the power constant for each window of 30 s ensures that a quasi-steady state is reached for the respective power setting. These stepwise increments are continued till the power reaches a maximum of 900 W. The system is held steady at a power of 900 W for a minute and then the process is reversed by reducing the power in decrements of 50 W every 30 s. It is seen that the system remains unstable even at 600 W during the decreasing power steps although the system was initially stable at 600 W as seen in Figure 3. Therefore, the decrements in power are continued till a lower bound of 200 W is reached as seen in Figure 5.

The top part in Figure 5 shows the profile of pressure signal for the above numerical experiment, while the bottom part shows the temporal variations in power and the average (wire) temperature of the two heaters in the Rijke tube apparatus: *P1* and *TWire1* for the primary heater, and *P2* and *TWire2* for the secondary (inactive) heater. It is seen that the temperature profile has a lag as compared to the heater power profile, which is an effect of the thermal dynamics; these phenomena have not been captured by most reduced-order numerical models. Figure 6 presents the hysteresis loop for the numerical experiment, where the changes in the RMS values (P_{rms}) of the pressure oscillations over the last 5 s of each 30 s window are shown along with the arrows that indicate the direction of the primary heater power being varied.

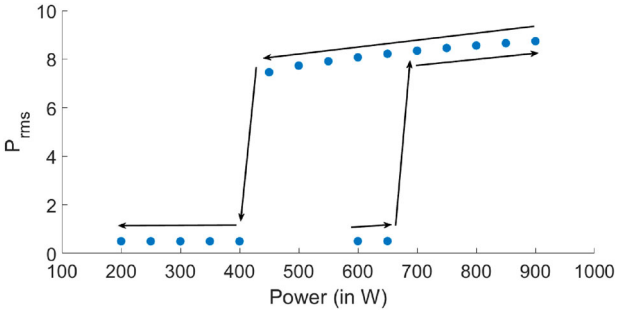

Figure 6. Hysteresis loop obtained from the simulation in Figure 5.

Following Figure 6, the system becomes unstable at ~ 700 W while the power is increased (i.e. forward path in the hysteresis diagram). However, as per the stability chart in Figure 3, this operational condition is expected to be stable. Further increasing the power to 900 W only increases the amplitude of the pressure oscillations, but the system still remains unstable. On the return path, however, the system stays unstable past 700 W and remains unstable right down till ~ 450 W. At ~ 400 W, the system finally returns to stability and remains stable for lower values of power. As seen in Figure 6, this leads to a reasonably large hysteresis loop, very similar to what was reported by [4].

5. Simulated control using the secondary heater

This section presents a numerical simulation of active control of the Rijke tube system by manipulating the power of the secondary heater while that of the primary heater is held constant. Having the dynamical model of the Rijke tube validated with experimental data, numerical simulations have been performed to test the efficacy of the secondary heater as a (passive) controller to suppress the thermoacoustic oscillations.

Usage of a secondary heat source for active control of thermoacoustic instabilities has been addressed in the technical literature (e.g. [20,26]. To this end, the researchers have placed a secondary electric heater downstream in the flow path of the Rijke tube to control the instabilities, where a Bunsen burner served as the primary heat source; this concept has been validated both numerically and experimentally. However, the numerical simulations have not included the heater dynamics and therefore yielded nearly instantaneous control, which is different from real-life experiments. The current paper has included the effects of heater dynamics and compared the results with the findings of [20]. In the current paper, all controllers are passive with no feedback loop because the primary aim is to show the effectiveness of the secondary heater for control of thermoacoustic pressure oscillations and the expected time delays due to the system dynamics.

5.1. *Simulated control: effectiveness of control heater*

In order to demonstrate its efficacy as a controller, the secondary heater has been placed at $x_2 = 1.125$ m, which is about three-quarters of the length down the Rijke tube. This location has been demonstrated by [4] to be most effective for suppressing thermoacoustic instabilities in the Rijke tube when the primary heater is placed at a quarter length down

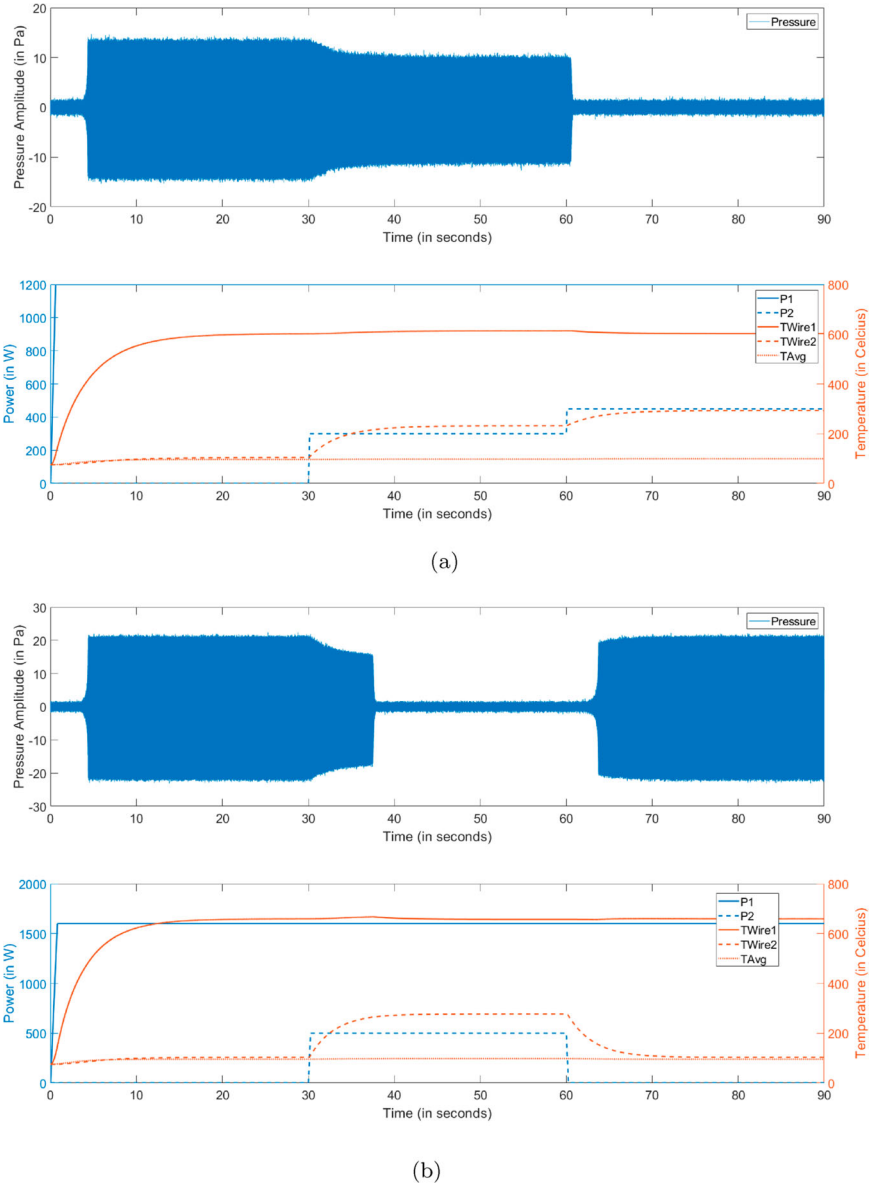

Figure 7. Time series of pressure, temperature, and power in two simulated control experiments. (a) Time series from the first control case: flow rate of 140 LPM and (b) time series from the second control case: Flow rate of 210 LPM.

from the inlet. Two trial cases are conducted to demonstrate the effects of the secondary heater and the results are shown in Figure 7.

The first case consists of numerical simulations for a time interval of 90 s with a constant flow rate of 140 LPM. At the very start (i.e. time $t = 0$ s), as the primary heater power is increased to 1200 W, the system becomes unstable. The primary power is then held at a constant level of 1200 W for 90 s, while leaving the secondary heater turned

off. At time $t = 30$ s, the secondary heater power is increased to 300 W and then further increased to 450 W at $t = 60$ s. The profiles of the corresponding pressure time series and associated power and temperature time series are shown in Figure 7(a). It is seen that although the secondary heater power at 300 W is incapable of completely suppressing the thermoacoustic instabilities, it modestly reduces the amplitude of the pressure oscillations. However, increasing the secondary power to 450W completely suppresses the high-amplitude pressure oscillations.

The second case consists of numerical simulations for a time interval of 90 s with a constant flow rate of 210 LPM. At time $t = 0$ s, the primary heater power is increased to 1600 W while the secondary heater is kept off till $t = 30$ s and then raised to 500 W; the secondary heater is switched off at $t = 60$ s. The corresponding pressure time series and the associated power and temperature time series are shown in Figure 7(b). It is seen that the initially unstable system is adequately controlled by switching on the secondary heater. However, when the secondary heater is switched off, the system reverts back to instability.

5.2. *Simulated control: effect of control heater location*

The location of the control (secondary) heater largely determines whether the instability would be successfully suppressed. To demonstrate this phenomenon, numerically, two cases have been considered, each having a simulated time interval of 460 s. In both cases, the air flow rate is kept constant at 180 LPM and, at $t = 0$ s, the primary heater power is raised to 1400 W; at $t = 20$ s, the secondary heater power is increased to 600 W. As seen in Figure 8(a), the instability is completely suppressed. Figure 8(b) shows that, although the amplitude is very modestly reduced, the pressure oscillations still prevail. This is due to the fact that the secondary heater is located at $x_2 = 1.125$ m (i.e. 3L/4 from inlet) for first case (Figure 8(a)), which is the most effective location for control. In contrast, for Figure 8(b), the secondary heater is placed further upstream at $x_2 = 0.875$ m (i.e. 7L/12 from inlet).

5.3. *Simulated control: comparison with results reported in technical literature*

In their research, [20] studied the effects of location of the secondary heater on suppression of thermoacoustic instabilities in a Rijke tube. It was observed that, for a particular operating condition, placing the secondary heater at 0.73 L causes the minimum power needed to mitigate instability to be 122.5 W in their apparatus. Placement of the secondary heater at 0.80 and 0.87 L causes the needed minimum power levels to be 183 and 309 W, respectively.

In the current paper, similar numerical simulations have been conducted for the flow rate of 210 LPM and primary power of 1200 W. When the secondary heater is placed at 0.73 L(1.095 m), the minimum power needed to completely suppress the oscillations is found to be $\sim$ 268 W; and when the heater is placed at 0.80 L(1.2 m)and 0.87 L(1.305 m), the minimum power requirements are $\sim$ 326 and $\sim$ 513 W, respectively. Thus, a very similar trend is observed between the numerical simulations presented in this paper and those generated experimentally by [20]. The values do not match exactly because of the following reasons. The Rijke tube geometries are different and the primary heat source in the experimental work by [20] is a flame while the heat source in the numerical model, presented in this paper, is an electric heater; hence the input conditions are dissimilar.

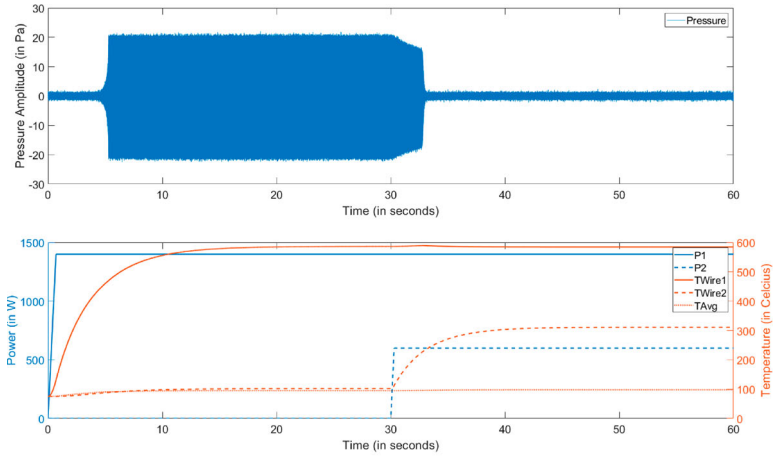

(a)

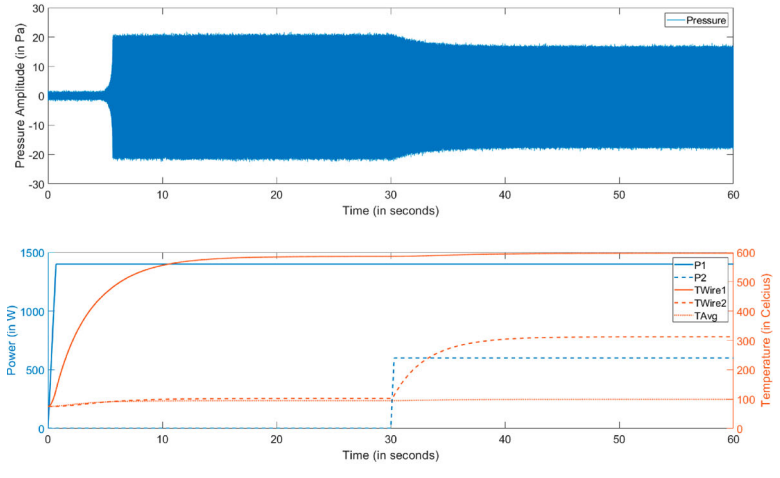

(b)

Figure 8. Effects of the control heater location on system dynamics. (a) Time series of pressure, temperature, and power in the simulation with the control heater placed at $x_2 = 1.125$ m (3L/4) and (b) time series of pressure, temperature, and power in the simulation with the control heater placed at $x_2 = 0.875$ m (7L/12).

6. Summary, conclusions, and future work

This paper has proposed a modification of the traditional Galerkin-mode-based technique to construct a reduced-order model of an (electrically heated) Rijke tube, which includes the inherent thermal physics of the heaters and the system dynamics in general. The model equations are developed by including the heat transfer phenomena in the heaters and thermoacoustics in the Rijke tube. This approach yields realistic time lags which are critical for evaluating dynamic performance and system stability for real-time monitoring and active control. The model structure is flexible in the sense that it is capable of incorporating either

a single heater or a combination of two heaters, where typically the secondary heater acts as an actuator for controlling the thermoacoustic instabilities.

The single-heater reduced-order model has been validated with experimental data collected from the Rijke tube apparatus, and the numerical results of the reduced-order model have yielded very good agreement with those obtained experimentally. The performance of the two-heater model has been tested by numerical simulation and is seen to function as expected. Numerical results of the two-heater model are compared with those of other available models, reported in open literature, which are also in good agreement. The numerical simulations show the effectiveness of the secondary heater as a (passive) controller.

The following topics are suggested for future research:

(1) Experimental validation of the two-heater model results on the Rijke tube apparatus.
(2) Detailed analysis of the fundamental frequencies in the system dynamics to serve as indicators of anomalous operations.
(3) Analysis and synthesis of a robust controller for real-time active control of thermoacoustic instabilities based on the two-heater numerical model.
(4) Implementation and testing of the above active controller on the Rijke tube apparatus.

Disclosure statement

No potential conflict of interest was reported by the authors.

Funding

The work reported here has been supported in part by the U.S. Air Force Office of Scientific Research (AFOSR) [grant numbers FA9550-15-1-0400 and FA9550-18-1-0135] in the area of dynamic data-driven application systems (DDDAS). The authors also thank Indo-US Science and Technology Forum (IUSSTF) for granting the Research Internship for Science and Engineering (RISE) scholarship to the first author for collaboration between Pennsylvania State University and Jadavpur University.

References

[1] J.W.S. Rayleigh, *The Theory of Sound*, Dover, New York, 1845.
[2] S. Candel, *Combustion dynamics and control: Progress and challenges*, Proc. Combust. Inst. 2(9) (2002), pp. 1–28.
[3] P.L. Rijke, *Notiz über eine neue art, die in einer an beiden enden offenen r̈hre enthaltene luft in schwingungen zu versetzen*, Ann. Phys. 18(3) (1859), pp. 339–343.
[4] K.I. Matveev, *Thermoacoustic instabilities in the rijke tube: Experiments and modeling*, Ph.D. diss., California Institute of Technology, 2003.
[5] L. Kabiraj and R.I. Sujith, *Nonlinear self-excited thermoacoustic oscillations: Intermittency and flame blowout*, J. Fluid. Mech. 71(3) (2012), pp. 376–397.
[6] D. Zhao, *Transient growth of flow disturbances in triggering a Rijke tube combustion instability*, Combust. Flame. 15(9) (2012), pp. 2126–2137.
[7] D. Zhao and Z.H. Chow, *Thermoacoustic instability of a laminar premixed flame in Rijke tube with a hydrodynamic region*, J. Sound. Vib. 33(2) (2013), pp. 3419–3437.
[8] A. Sjunnesson, P. Henrikson, and C. Lofstrom, *CARS measurements and visualization of reacting flows in a bluff body stabilized flame*, in *28th Joint Propulsion Conference and Exhibit, Joint Propulsion Conferences*, 1992.
[9] A. Fichera, C. Losenno, and A. Pagano, *Experimental analysis of thermo-acoustic combustion instability*, Appl. Energy. 7 (2001), pp. 179–191.

[10] J.G. Lee and D.A. Santavicca, *Experimental diagnostics for the study of combustion instabilities in lean premixed combustors*, J. Propul. Power 1(9) (2003), pp. 735–750.
[11] F. Richecoeur, S. Ducruix, P. Scouflaire and S. Candel, *Experimental investigation of high-frequency combustion instabilities in liquid rocket engine*, Acta. Astronaut. 6(2) (2008), pp. 18–27.
[12] U. Sen, T. Gangopadhyay, C. Bhattacharya, A. Misra, P.S.S. Karmakar, A. Mukhopadhyay, and S. Sen, *Investigation of ducted inverse nonpremixed flame using dynamic systems approach*, in *ASME Turbo Expo 2016: Turbomachinery Technical Conference and Exposition*, Vol. 4B, 2016.
[13] F.E.C. Culick, *Nonlinear behavior of acoustic waves in combustion chambers-I*, Acta. Astronaut. 3 (1976), pp. 715–734.
[14] M.A. Heckl, *Active control of the noise from a Rijke tube*, J. Sound. Vib. 12(4) (1988), pp. 117–133.
[15] M.A. Heckl, *Non-linear acoustic effects in the Rijke tube*, Acustica 7(2) (1990), pp. 63–71.
[16] P. Subramanian, S. Mariappan, R.I. Sujith, and P. Wahi, *Bifurcation analysis of thermoacoustic instability in a horizontal rijke tube*, Int. J. Spray Combust. Dyn. 2 (2010), pp. 325–355.
[17] G.A. Richards, D.L. Straub, and E.H. Robey, *Passive control of combustion dynamics in stationary gas turbines*, J. Propul. Power 1(9) (2003), pp. 795–810.
[18] D. Zhao and A. Morgans, *Tuned passive control of combustion instabilities using multiple Helmholtz resonators*, J. Sound. Vib. 32 (2009), pp. 744–757.
[19] N.N. Deshmukh and S. Sharma, *Experiments on heat content inside a Rijke tube with suppression of thermo-acoustics instability*, Int. J. Spray Combust. Dyn. 9 (2017), pp. 85–101.
[20] D. Zhao, C. Ji, X. Li, and S. Li, *Mitigation of premixed flame-sustained thermoacoustic oscillations using an electrical heater*, Int. J. Heat. Mass. Transf.8(6) (2015), pp. 309–318.
[21] S. Mondal, N.F. Ghalyan, A. Ray, and A. Mukhopadhyay, *Early detection of thermoacoustic instabilities using hidden Markov models*, Combust. Sci. Technol.19(1) (2019), pp. 1309–1336.
[22] F.E.C. Culick, *Combustion instabilities in liquid-fuelled propulsion systems*, AGARD-CP-450, 1988.
[23] K.I. Matveev and F.E.C. Culick, *A model for combustion instability involving vortex shedding*, Combust. Sci. Technol. 17(5) (2003), pp. 1059–1083.
[24] V. Nair, R.I. Sujith, *A reduced-order model for the onset of combustion instability: Physical mechanisms for intermittency and precursors*, in *Proceedings of the Combustion Institute*, Vol. 35, 2015, pp. 3193–3200
[25] J.R. Andrews, *Temperature Dependence of Gas Properties in Polynomial Form*, The NPS Institutional Archive DSpace Repository, Calhoun, 1981.
[26] X. Jin, H. Zhao and S. Li, *Experimental and numerical study of passive control of self-sustained thermoacoustic oscillations using an electrical heater*, Energy Procedia 105 (2017), pp. 4661–4667. 8th International Conference on Applied Energy, ICAE2016, 8–11 October 2016, Beijing, China.